NASA Technical Memorandum 107734

CHARACTERISTICS OF VERTICAL AND LATERAL TUNNEL TURBULENCE MEASURED IN AIR IN THE LANGLEY TRANSONIC DYNAMICS TUNNEL

**Robert K. Sleeper, Donald F. Keller,
Boyd Perry III, and Maynard C. Sandford**

March 1993

National Aeronautics and
Space Administration

Langley Research Center
Hampton, Virginia 23681-0001

CHARACTERISTICS OF VERTICAL AND LATERAL TUNNEL TURBULENCE MEASURED IN AIR IN THE LANGLEY TRANSONIC DYNAMICS TUNNEL

By

Robert K. Sleeper, Donald F. Keller, Boyd Perry III,
and Maynard C. Sandford
NASA Langley Research Center

ABSTRACT

Preliminary measurements of the vertical and lateral velocity components of tunnel turbulence were obtained in the Langley Transonic Dynamics Tunnel test section using a constant-temperature anemometer equipped with a hot-film X-probe. For these tests air was the test medium. Test conditions included tunnel velocities ranging from 100 to 500 fps at atmospheric pressure. Standard deviations of turbulence velocities were determined and power spectra were computed. Unconstrained optimization was employed to determine parameter values of a general spectral model of a form similar to that used to describe atmospheric turbulence. These parameters, and others (notably break frequency and integral scale length) were determined at each test condition and compared with those of Dryden and Von Kármán atmospheric turbulence spectra. When data were discovered to be aliased, the spectral model was modified to account for and "eliminate" the aliasing.

INTRODUCTION

The Langley Transonic Dynamics Tunnel (TDT) is a closed-circuit, continuous-flow, slotted-throat wind tunnel capable of testing in air or heavy gas at total or stagnation pressures ranging from one atmosphere to near vacuum and over a Mach number range from near zero to 1.2. The test section of the TDT is 16 feet square and has cropped corners. This facility was designed to fill the need for a transonic wind tunnel capable of testing dynamic models of a size large enough to allow simulation of important structural properties of aircraft or spacecraft. Aeroelastic research conducted in the TDT includes the study of flutter, aerodynamic loads, forced response, and active controls (unpublished information contained in Langley Working Paper 799, "The Langley Transonic Dynamics Tunnel," dated September 23, 1969 with an updated reprint dated April 1992). An important consideration in the study of forced response and active controls is knowledge of the turbulence in the test section. Seven examples of wind-tunnel test programs involving aeroelastic models with active controls are shown in figure 1. Six of the seven are shown in the TDT and represent a cross-section of the variety and complexity of wind-tunnel models which could have benefited from knowledge of the turbulence in the test section.

This paper describes the first phase of a program to define the turbulence in the TDT. In this phase, vertical and lateral components of turbulence were measured in air at one total pressure only (atmospheric) and for a limited number of Mach numbers. Later the same turbulence components will be measured in air and in heavy gas at many combinations of total pressure and Mach number. Power spectral density functions of the two components of turbulence, and related statistical quantities, are computed from the measured data and "define the turbulence." It is hoped

that the information contained herein will be useful to control-law design engineers as they design control laws to be tested on active-controls models in the TDT.

A unique aspect of this program is the application of unconstrained optimization to determine the values of parameters that mathematically define the power spectral density functions of the velocity components at each test condition. One of the sections of this paper addresses the use of an unconstrained optimization procedure and the appendix to this paper describes certain aspects of a modified power spectral density function definition introduced after aliasing was discovered in the digitized data.

SYMBOLS

f	frequency, Hz
f_b	break frequency, Hz
$\bar{f}_b$	normalized break frequency
f_N	Nyquist frequency, Hz
k	summation index
L	integral scale length, ft
MSR	mean square ratio
n	spectral model denominator exponent
Obj	objective function
q	dynamic pressure, $\rho V^2/2$, psf
r	correlation coefficient
V	tunnel velocity, fps
α	spectral model amplitude, $(fps)^2/Hz$
β	spectral model numerator coefficient, sec^2
β'	nondimensional spectral model numerator coefficient
γ	spectral model denominator coefficient, sec^2
γ'	nondimensional spectral model denominator coefficient
ϕ	unaliased turbulence spectrum, $(fps)^2/Hz$
ϕ_A	aliased turbulence spectrum, $(fps)^2/Hz$
ϕ_{meas}	measured turbulence spectrum, $(fps)^2/Hz$
ρ	fluid density, $slugs/ft^3$
σ	standard deviation, fps

APPARATUS

The apparatus consisted of the following components:

Transonic Dynamics Tunnel (TDT)

The features and characteristics of the TDT are described in detail in LWP-799. Figure 2 shows an aerial view of the TDT facility; figure 3 shows a plan view drawing. A sting, identified in figure 12 of LWP-799 as "Sting 6," was used to support an X-probe on the centerline of the TDT test section at longitudinal station 72, the position where the center-of-gravity of wind-tunnel models is located for most tests. The sting could be inclined in pitch about its forward tip as shown in the multiple-exposure photograph in figure 4. This feature was used in calibrating the X-probe.

Tunnel Instrumentation

The following information was available from tunnel instrumentation: flow velocity, Mach number, total temperature, sting pitch angle, and static, dynamic and total pressures. Time-averaged values of these quantities, based on a sample rate of 4 samples per second over a duration of 15 seconds, were available.

Anemometry System

Figure 5 shows the two major components of the anemometry system: an anemometer console and a cross- or X-probe. The probe is shown greatly magnified. The probe contains two filaments arranged in an X-pattern and separated by 0.04 inches. The filaments are mutually perpendicular and each is aligned at 45° with respect to the axis of the probe. For durability, film filaments, which are constructed by bonding a thin film of platinum onto the surface of a fused quartz substrate, were chosen over wire filaments. The film filaments were about 0.08 inches long and 0.002 inches in diameter. A view of the X-probe showing its actual size is presented in figure 6. In figure 7 the X-probe is shown in the TDT test section mounted at the end of Sting 6. The X-probe was mounted on the sting in such a manner that it could be rotated about its axis.

The anemometer measured voltage variations, over a broad frequency range, from each filament of the X-probe. A dummy probe was used to provide a measure of the cable resistance. The characteristics of the electrical cables that connected the probes to the anemometer met manufacturer's specifications. Voltages from the X-probe were calibrated to provide both components of flow velocities in a plane that includes the probe axis. (The probe is insensitive to flow normal to this plane.) The pair of anemometer voltage signals and their difference were sampled at 200 samples per second, yielding a Nyquist frequency of 100 Hz.

Other Instrumentation

In anticipation of possible sting motion due to vibrations, the sting was instrumented with accelerometers. These possible sting motions, if large enough, could have contaminated the readings from the anemometer since an anemometer cannot distinguish between voltages produced by the passage of moving air over a stationary X-probe and voltages produced by the passage of a moving X-probe through stationary air. Accelerations of the sting give an indication of sting motion and were used to determine if there was contamination. Such contamination would be manifested as additional power in the spectral density functions at the vibrational frequencies. The accelerations were sampled at 200 samples per second.

Overall System

The overall system, including instrumentation and data acquisition devices, is schematically illustrated in figure 8. A dual-trace oscilloscope was used to monitor the anemometer signals and the spectrum analyzer was used for on-line evaluation of the data measurements. All data were passed through a 1000 Hz low-pass filter before being saved digitally (at the respective sample rates noted above) on the MODCOMP data acquisition computer.

TEST PROCEDURE

A test procedure that minimized test time was employed. The procedure involved systematically alternating between acquiring data that would later be used to calibrate the anemometer (calibration data) and acquiring data that would later be reduced using the results from calibration (test data). Data for the vertical component of tunnel turbulence which included

calibration data were acquired before those of the lateral component. There were eleven calibration conditions and nine test conditions.

Figure 9 is a semilog plot of dynamic pressure as a function of Mach number and shows the TDT operating boundary for air. The various arching curves are contours of constant total pressure. The TDT operates along these contours as motor speed varies. All calibration and test conditions were on the atmospheric total pressure curve (2200 psf). The calibration conditions covered the range of tunnel velocities from 50 fps to 550 fps in increments of 50 fps. The test conditions, shown in the figure by open circles, covered the range of tunnel velocities from 100 fps to 500 fps, also in 50 fps increments. Corresponding ranges for Mach number and dynamic pressure for the test conditions are from 0.09 to 0.44 and from 11 psf to 250 psf, respectively.

Acquiring Data

Calibration data were recorded in tests of 15-second duration and test data in tests of 3-minute duration. Time-averaged tunnel instrumentation values were provided at the initiation and the termination of data tests to monitor the extent of value changes during tests. Calibration data and test data consisted of voltage outputs from the two filaments of the X-probe. Calibration data were acquired at known values of tunnel velocity and sting pitch angles over the angle range from -5° to +5° in increments of 1°. This range of sting pitch angles is depicted in figure 4. When the sting pitch angle was set to 0°, test data for the vertical component of tunnel turbulence were acquired. Tunnel velocity was then changed and this process was repeated.

After all calibration data and test data were acquired for the vertical component of tunnel turbulence, the X-probe was rotated 90° about its axis, the sting pitch angle was set to 0°, and, without further calibration, test data for the lateral component of tunnel turbulence were acquired at all tunnel velocities.

CALIBRATION

The mean tunnel flow at the location of the X-probe was assumed to be along the centerline of the test section.

After data acquisition, the next task was to apply the calibration in the conversion of the filament voltages to flow velocities. First, a grid of filament voltages for the calibration tunnel velocities and sting pitch angles was constructed. Next, linear regression was applied to provide smooth voltage variations with angle change at each velocity. Then, a table look-up procedure similar to that of reference 1 was employed to interpolate or extrapolate the turbulence velocity components from the measured voltage time histories (test data).

Figure 10 shows the linearized X-probe calibration results expressed in terms of a grid of filament voltages. The filament-voltage scales are identified by their attitude angles with respect to the probe axis. The figure shows a general increase in voltage for both filaments with velocity and small regular, negatively-sloped changes in voltages due to pitch angle. At the higher velocities, the slopes of the changes due to pitch angle become more negative.

The process of calibration was conducted in the vertical plane while the plane of response of the X-probe was aligned vertically. The vertical calibration was also applied to the lateral measurements since the probe was merely rotated for the lateral measurements. Thus, both the velocity components were converted from voltages using the calibration relationships derived from the vertical measurements.

DATA REDUCTION

Except for some on-line measurements which will be described next, all data reduction was performed subsequent to testing.

On-Line Data Examination

At each test condition on-line measurements were made of power spectral density functions of the difference in voltages between the two probe filaments. For an ideal X-probe, reference 2 shows that this voltage difference is proportional to the measured flow normal to the probe axis. In addition, on-line measurements were made of power spectral density functions of the sting accelerations. These spectra were characterized by prominent peaks at the frequencies of vibration of the sting. The voltage-difference spectra were examined for peaks at these same frequencies, but none were found. Had such peaks been found, the conclusion would have been made that the motion of the sting was responsible for those peaks and that contamination existed. However, because this condition did not exist, it was judged that no contamination existed.

Turbulence-Velocity Time Histories

Total-velocity time histories were determined from filament voltage time histories by employing the calibration procedure discussed previously. Turbulence-velocity time histories were then obtained from the total-velocity time histories by subtracting the mean from the velocity components.

Standard deviations of each component of tunnel turbulence were computed from the turbulence-velocity time histories. The turbulence levels, expressed as a percentage of tunnel velocity, were computed by dividing the standard deviations by the corresponding tunnel velocities.

Turbulence-Velocity Power Spectral Density Functions

Power spectral density functions of the vertical and lateral components of tunnel turbulence were computed from the turbulence-velocity time histories using the Blackman-Tukey method (ref. 3). In this method an estimate of the autocorrelation function for each time history is computed first. These autocorrelation functions were chosen to have 512 lags. Next, for each autocorrelation function, a Hanning lag window was employed and an estimate of the power spectral density function was computed.

When the resulting power spectral density functions exhibited the characteristic inflections in the spectra at frequencies approaching the Nyquist frequency, aliasing was determined to be present in the digitized data.

Use of Unconstrained Optimization to Approximate Measured Spectra

An important objective of the program was to determine the values of parameters α, β, γ, and n within the following assumed simple analytical expression which approximates the measured tunnel-turbulence power spectra at each test condition

$$\phi(f) = \alpha \frac{1+\beta f^2}{\left(1+\gamma f^2\right)^n} \qquad (1)$$

This expression was chosen because it is consistent with and has properties similar to the familiar Dryden and Von Kármán forms of atmospheric-turbulence power spectra. In choosing equation (1), the authors hoped to use their understanding of the familiar forms of atmospheric-turbulence power spectra to interpret the characteristics of the tunnel-turbulence power spectra.

An important property of equation (1) is its asymptotic behavior. At low values of frequency the value of ϕ asymptotically approaches a constant value, and at high values of frequency the value of ϕ asymptotically approaches zero as the negative 2(n-1) power of frequency. On a log-log plot, these low- and high-frequency asymptotes are straight lines with slopes of zero and negative 2(n-1), respectively. At intermediate values of frequency there is a transition between the low- and high-frequency asymptotes in the vicinity of a frequency which will be referred to as the break frequency, f_b. The quantity f_b is defined to be the frequency at which the low- and high-frequency asymptotes intersect and is expressed as

$$f_b = \left(\frac{\beta}{\gamma^n}\right)^{1/2(n-1)} \tag{2}$$

Before the presence of aliasing was detected, the authors had conceived a straightforward procedure, which employed unconstrained optimization, to determine the parameters α, β, γ, and n. In this procedure these four parameters were the design variables and the objective function was based on the difference between equation (1) and the measured power spectrum, over the frequency range of zero to the Nyquist frequency. The procedure assumed that there was no aliasing present in the measured data, therefore, ϕ in equation (1) is referred to as the unaliased spectral model.

The objective function was the sum, over the frequency range from zero to the Nyquist frequency, of the square of the differences of the logarithms of the unaliased spectral model and the measured spectrum

$$\text{Obj} = \sum_f \left\{\log[\phi_{meas}(f)] - \log[\phi(f)]\right\}^2 \tag{3}$$

The difference in logarithms of spectra, rather than the difference of spectra, was chosen to force the optimizer to work as hard in the high-frequency region as it does on other portions of the spectrum. Because aliasing was discovered before optimization was performed, equation (3) was never employed, but an alternate form, to be described next, was employed.

"Eliminating" Aliasing

After the presence of aliasing was detected, the spectral model was modified to reflect the presence of aliasing. The design variables were the same but the objective function was based on the difference between the analytical expression, as specified in equation (4), and the measured power spectrum. The new analytical expression is referred to as the aliased spectral model and is comprised of the sum of all unaliased spectral segments (each segment based on eq. (1)) between zero and 1000 Hz, but "folded" about frequencies zero and the Nyquist frequency, f_N (refs. 3 and 5).

$$\phi_A(f) = \sum_k \alpha \frac{1+\beta(f+2kf_N)^2}{\left[1+\gamma(f+2kf_N)^2\right]^n} \tag{4}$$

$$\text{for } k = 0, \mp 1, \mp 2, \mp 3, \ldots$$

When aliasing is considered, the expression for $\phi_A(f)$ in equation (4) replaces $\phi(f)$ in the objective function yielding,

$$Obj = \sum_f \left\{ \log[\phi_{meas}(f)] - \log[\phi_A(f)] \right\}^2 \tag{5}$$

Parameters α, β, γ, and n were obtained during the optimization procedure. The Appendix to this paper describes the composition of equation (4) and provides an illustration of its validation to turbulence spectra.

Quantities Which "Define" the Turbulence

Equation (1) may be rewritten in a form identical to the Dryden and Von Kármán forms of reference 4, in terms of quantities V (velocity), L (turbulence integral scale length), and σ (turbulence standard deviation). Both forms of atmospheric-turbulence power spectra may be expressed in the following form

$$\phi(f) = \frac{\sigma^2 2L}{V} \frac{1 + \beta' \left(\frac{2\pi L}{V} \right)^2 f^2}{\left[1 + \gamma' \left(\frac{2\pi L}{V} \right)^2 f^2 \right]^n} \tag{6}$$

In comparing equations (1) and (6) term by term the following relationships are apparent:

$$\alpha = \frac{\sigma^2 2L}{V} \tag{7}$$

$$\beta = \beta' \left(\frac{2\pi L}{V} \right)^2 \tag{8}$$

$$\gamma = \gamma' \left(\frac{2\pi L}{V} \right)^2 \tag{9}$$

$$n = n \tag{10}$$

Quantities β' and γ' are nondimensional. A nondimensional break frequency may be defined as

$$\bar{f}_b = \left(\frac{2\pi L}{V} \right) f_b = \left(\frac{\beta'}{\gamma'^n} \right)^{1/2(n-1)} \tag{11}$$

Equations (1) and (6) both define the turbulence, but equation (6) will be used exclusively for the remainder of this paper because it is identical in form to the Dryden and Von Kármán forms. Therefore, knowledge of quantities σ, L, β', γ', n, and $\bar{f}_b$ is required to define the turbulence. These quantities are computed in the following manner: parameters α, β, γ, and n are determined using equation (5) as the objective function; quantity σ is computed from the turbulence-velocity time histories; and quantity V is known from the test conditions. With these

six quantities known, quantity L is computed using equation (7); quantities β' and γ' are computed using equations (8) and (9), respectively; and $\bar{f}_b$ is computed using equations (2) and (11).

RESULTS AND DISCUSSION

Table 1 contains a summary of the results which are discussed in this section of the paper. Also included in the table are the tab point, corresponding tunnel velocity, and dynamic pressure for each entry.

Turbulence-Velocity Standard Deviations

The standard deviations, which are a measure of the intensity of tunnel turbulence, were computed for the vertical and lateral components of tunnel turbulence. The vertical component is plotted in figure 11(a) as a function of tunnel velocity and in figure 11(b) as a function of dynamic pressure; the lateral component is similarly displayed in figure 12. As expected, the standard deviations tended to increase with both tunnel velocity and dynamic pressure, although the standard deviations of the vertical component were slightly greater than those of the lateral component. The maximum standard deviation for the vertical component was about 3.5 fps; for the lateral component, about 3.1 fps.

Some discrepancies in the data were noted. For the vertical component of tunnel turbulence at a tunnel velocity of 500 fps three sample records were obtained, resulting in three significantly different values of standard deviation. At a tunnel velocity of 300 fps there appears to be a condition of low turbulence intensity for both components of tunnel turbulence. These discrepancies were investigated but no apparent reason for them was found. These will be investigated further in the next phase of the program.

Also plotted in figures 11 and 12 are the linear least squares estimates constrained to pass through the origin. The correlation coefficient, r, of each estimate is indicated on the plot. For both components of tunnel turbulence, the correlation coefficient is somewhat greater when the data are plotted as a function of dynamic pressure, suggesting a slightly stronger linear relationship with dynamic pressure than with velocity.

Tunnel turbulence is frequently expressed as a percent of tunnel velocity. The data of figures 11 and 12 were normalized by tunnel velocity and then replotted in figures 13 and 14. For the vertical component, the percentages ranged from about 0.2 % to about 0.8 % of tunnel velocity. For the lateral component the percentages ranged from about 0.3 % to about 0.6 %. The figures also include linear least squares estimates.

Turbulence-Velocity Power Spectral Density Functions

Figure 15 (a-k) contains eleven log-log plots of the power spectral density functions of the vertical component of tunnel turbulence for the different tab points and tunnel velocities. Figure 16 (a-j) contains ten similar plots for the lateral component. To aid in comparing the power spectra the scales on all 21 plots were kept identical.

Each plot contains the following:

(1) An estimate of the power spectral density function computed from the turbulence-velocity time history.
The estimate is characterized by jaggedness and by aliasing.
It is labeled on the plot as "measured spectrum."

(2) The aliased spectral model (eq. (4)), obtained by performing the optimization procedure.
It is generally difficult to see this model representation on the plot because it passes through the middle of the measured spectrum, an indication of the success of the optimization procedure.
It is labeled on the plot as "aliased spectral model."

(3) The unaliased spectral model (eqs.(1) and (6)), obtained by substituting into equation (1) the optimized values of the parameters from the aliased spectral model.
This model is always below the corresponding aliased spectral model for all frequencies.
It is labeled on the plot as "unaliased spectral model."

The measured spectra exhibit trends with increasing tunnel velocity consistent with the corresponding trends for standard deviation. For instance, as tunnel velocity is increased from 100 fps to 500 fps there is about an order-of-magnitude increase in the standard deviation for both components of turbulence. There is also about an order-of-magnitude increase in the low-frequency values of the measured spectra.

For the present application, an indication of the amount of aliasing present in a measured spectrum is the difference in the magnitudes of the low-frequency asymptotes of the aliased and unaliased spectral models. A relatively small difference, as in figures 15(a) and 16(a), indicates a relatively small amount of aliasing. A relatively large difference, as in figures 15(j) and 16(g), indicates a relatively large amount of aliasing. The mean square ratio (MSR) provides a quantitative measure of the error present in the power spectra due to aliasing; the smaller the MSR, the greater the error. The MSR is the ratio of the areas under the unaliased and aliased power spectra from the lowest frequency to the Nyquist frequency. For the twenty one spectra obtained in the present study, the ratios ranged from 0.624 to 0.861.

Quantities Which "Define" the Turbulence

Figures 17 and 18 contain plots, as functions of tunnel velocity, of the quantities which define the turbulence. Figure 17 displays the quantities for the vertical component of tunnel turbulence; figure 18, the lateral component. The quantities plotted are α, β', γ', the ratio β'/γ', n, L, and $\bar{f}_b$. Where appropriate, for comparison with atmospheric turbulence power spectra, the values of the quantities from the Dryden and Von Kármán forms are indicated on the plot. Each plot contains a least-squares line through the data.

Because the general trends in corresponding data in figures 17 and 18 are very similar, the following discussion applies to both the vertical and lateral components of tunnel turbulence.

Amplitude α.- Figures 17(a) and 18(a) show variations of α with tunnel velocity, variations which have a similar character to those of σ in figures 11(a) and 12(a). (From equation (7), for a given velocity and a given value of L, α is proportional to the square of σ.) The least-squares line in these plots was constrained to pass through the origin.

Coefficient β'.- Figures 17(b) and 18(b) show variations of β' with tunnel velocity. The least-squares line has a very shallow positive slope, indicating that the value of β' is very nearly constant with tunnel velocity. Corresponding values of β' from the Dryden and Von Kármán forms, 3 and 4.781, respectively, are about an order of magnitude larger than the values of β' from tunnel turbulence. This discrepancy in β' may be related to the physical restraints that the tunnel walls impose on the flow, restraints that are not present in the atmosphere.

Coefficient γ'.- Figures 17(c) and 18(c) show variations of γ' with tunnel velocity. The least-squares line here also has a very shallow positive slope, also indicating that the value of γ' is very nearly constant with tunnel velocity. Corresponding values of γ' from the Dryden and Von Kármán forms, 1 and 1.793, respectively, are about two to four times larger than the values of γ' from tunnel turbulence. This discrepancy in γ' may also be related to the physical restraints that the tunnel walls impose on the flow, restraints that are not present in the atmosphere.

Ratio β' / γ'.- Figures 17(d) and 18(d) show variations of the parameter ratio β'/γ' with tunnel velocity. The least-squares line again has a very shallow positive slope, indicating, again, that the value of β'/γ' is very nearly constant with tunnel velocity. Corresponding values of β'/γ' from the Dryden and Von Kármán forms, 3 and 2.667, respectively, are about three times larger than the values of β'/γ' from tunnel turbulence.

Exponent, n.- Figures 17(e) and 18(e) show variations of the exponent n with tunnel velocity. The least-squares line is essentially horizontal, indicating that the value of n is constant with tunnel velocity. Corresponding values of n from the Dryden and Von Kármán forms, 2 and 1.833, respectively, are extremely close to the values of n from tunnel turbulence.

Normalized break frequency, $\bar{f}_b$.- Figures 17(f) and 18(f) show variations of $\bar{f}_b$ with tunnel velocity. The least-squares line again has a very shallow positive slope, indicating, again, that the value of $\bar{f}_b$ is very nearly constant with tunnel velocity. Corresponding values of $\bar{f}_b$ from the Dryden and Von Kármán forms, 1.732 and 1.345, respectively, are extremely close to the values of $\bar{f}_b$ from tunnel turbulence. From equation (11), for a constant normalized break frequency and a constant value of L, the (unnormalized) break frequency will be proportional to tunnel velocity.

Integral scale length, L.- Figures 17(g) and 18(g) show variations of L with tunnel velocity. The least-squares line has a very shallow positive slope, indicating that the value of L is very nearly constant with tunnel velocity. Typical values of L from the Dryden and Von Kármán forms are 1000 and 2500, respectively. For atmospheric turbulence the quantity L is interpreted as the average diameter of the largest eddies in the atmosphere (ref. 4). If a similar interpretation were made for tunnel turbulence, the largest eddies could not be larger than the test section size. For tunnel turbulence, as indicated in figures 17(g) and 18(g), the value of L was about 4 feet, more than two orders of magnitude below the typical values for atmospheric turbulence, but, more importantly, smaller than the 16-foot test section size and therefore consistent with the interpretation of integral scale length and eddy size.

All of these so called "defining" quantities exhibit only small differences with measurement direction, suggesting that the turbulence within the test section of the TDT may be isotropic, i.e., independent of direction.

CONCLUDING REMARKS

Preliminary measurements of the vertical and lateral velocity components of tunnel turbulence were obtained in the Langley Transonic Dynamics Tunnel test section using a constant-temperature anemometer equipped with a hot-film X-probe. For these tests air was the test medium. Test conditions included tunnel velocities ranging from 100 to 500 fps at atmospheric pressure. Standard deviations of vertical and lateral turbulence velocity components were determined and power spectra were computed. Both components of turbulence generally increased with tunnel velocity. In terms of percentages of tunnel velocity, the intensity of the tunnel

turbulence ranged from about 0.2% to 0.8% for the vertical component, and ranged from about 0.3% to about 0.6% for the lateral component. Unconstrained optimization was employed to determine the values of parameters within simple analytical expressions for the power spectra. When data were discovered to be aliased, the spectral model form was modified to account for and "eliminate" the aliasing. Excellent agreement between the modified model and the measured velocity spectra was achieved. The parameters completely define the power spectral density function of turbulence for each component of turbulence at each tunnel velocity. From these parameters break frequency and integral scale length were determined at each test condition. These quantities were compared with those of Dryden and Von Kármán atmospheric-turbulence power spectra.

APPENDIX

THE ALIASED SPECTRAL MODEL

This appendix offers more information about the aliased spectral model, equation (4) in the main body of the paper.

Aliased Spectrum Defined in Terms of Unaliased Spectrum

Assume that a random process exists whose (unaliased) power spectrum is expressed by equation (1) from the main body of the paper, repeated here as equation (A1)

$$\phi(f) = \alpha \frac{1+\beta f^2}{\left(1+\gamma f^2\right)^n} \qquad \text{(A1)}$$

The range of frequency, f, in equation (A1) is zero to infinity. When this equation is plotted in a log-log format, it has a shape as shown by the unaliased spectrum of figure A1.

Assume also that a sampled record of this random process (with Nyquist frequency, f_N) has been obtained and that a power spectrum has been computed from the sampled record. Assume, further, that this computed power spectrum exhibits evidence of aliasing, notably a "curling up" at frequencies approaching f_N. This aliased spectrum has a shape as shown by the aliased spectrum of figure A1

As shown in such references as 3 and 5, an aliased power spectrum, over its frequency range of zero to f_N, contains all the power of the unaliased power spectrum, over its frequency range of zero to infinity. The aliased power spectrum may be expressed as an infinite "folded" sum of spectral segments of the unaliased power spectrum. Equation (4) from the main body of the paper expresses this sum and is repeated here as equation (A2)

$$\phi_A(f) = \sum_k \alpha \frac{1+\beta\left(f+2kf_N\right)^2}{\left[1+\gamma\left(f+2kf_N\right)^2\right]^n} \qquad \text{(A2)}$$

$$\text{for } k = 0, \mp 1, \mp 2, \mp 3, \ldots$$

The range of frequency, f, in equation (A2) is zero to f_N.

Figure A2 contains a sketch illustrating the composition of an aliased spectrum in terms of the sum of the folded segments of its corresponding unaliased spectrum. For ease in visualizing a sum, figure A2 is in linear-linear format. In the figure, the aliased and unaliased spectra are labeled and the folded segments are seen folding back and forth between zero and f_N. While the sum actually includes an infinite number of segments, for purposes of illustration, only three segments are shown in the figure, corresponding to k=0, k=-1, and k=+1 in equation (A2). Each segment has a bandwidth, or frequency range, equal to f_N. The contribution to the sum from each successive segment becomes successively smaller. This fact raises the question: Recognizing that the 1000 Hz low-pass filter imposes an upper limit of 10 segments, how many folded spectral segments are required to converge to the measured spectrum?

Figure A3 illustrates the results from a study that was performed to determine the number of folded spectral segments to include in the optimization procedure. Figure A3 is a magnified view of the high-frequency portion of the power spectrum in figure 16(g), chosen because it contains a significant amount of aliasing. The various dashed curves in the figure represent increasing numbers of spectral segments included in equation (A2). The lowest dashed curve corresponds to k=-1 in equation (A2) (or, the primary spectral segment plus one additional spectral segment); the highest dashed curve corresponds to k=-5 (or, the primary plus nine additional segments). These two extremes correspond to upper limits of frequency of $2f_N$ and $10f_N$, respectively. The upper limit of $10f_N$ is seen to give the best agreement between the aliased spectral model and the measured spectrum, and for this reason, $10f_N$ was chosen as the upper limit for all optimizations. In figure A3 the smooth solid line below the lowest dashed line is the unaliased spectral model, corresponding to the aliased spectral model with upper limit of frequency of $10f_N$.

Validation of Aliased Spectral Model

To validate the procedure for "eliminating" aliasing, a numerical test was performed on a Dryden power spectral density function deliberately aliased by creating a sampled analytical autocorrelation function. For a theoretical and unaliased Dryden power spectrum, expressed in the form of equation (6), the values of β', γ', and n are 3, 1, and 2, respectively. For this numerical test, values of σ, L and V were arbitrarily chosen to be 2, 4, and 400 respectively. Therefore, from equations (7), (8), and (9), the values of α, β, and γ were 0.0800, 0.01184, and 0.00395 respectively.

Using the optimization procedure on this deliberately aliased spectrum, the unconstrained optimizer determined the values of α, β, γ, and n to be 0.0802, 0.01210, 0.00406, and 1.98, respectively. Because the largest difference between these values and the theoretical values was only 3%, this numerical test was judged to successfully validate the procedure.

ACKNOWLEDGMENTS

The authors wish to acknowledge the data reduction effort of Kurt M. Hitke of the UNISYS Corporation and the helpful suggestions of Anthony S. Pototzky of the Lockheed Engineering & Sciences Company.

REFERENCES

1. Lueptow, R. M.; Breuer, K. S.; and Haritonidis, J. H.: Computer-aided Calibration of X-probes Using a Look-up Table. Experiments in Fluids 6, pp 115-118, Springer-Verlag, 1988.

2. Nystrom, Lowell D.: Anemometry. Technical Bulletin TB5. TSI Incorporated, Oct. 1970.

3. Otnes, Robert K.; and Enochson, Loren: Applied Time Series Analysis. John Wiley and Sons, Inc., 1978.

4. Houbolt, John C.; Steiner, Roy; and Pratt, Kermit G.: Dynamic Response of Airplanes to Atmospheric Turbulence Including Flight Data on Input and Response. NASA TR-199, 1964.

5. Bendat, Julius S.; and Piersol, Allan G.: Random Data. Second edition. John Wiley and Sons, Inc., 1986.

Table 1.- Summary of Tunnel Turbulence Characteristics

Velocity	Test Tab Point	Dynamic Pressure	Standard Deviation	Turbulence	Mean Square Ratio	Spectrum Model Parameters					Normalized Break Freq	Integral Scale Length
						Amplitude Coefficient	Coefficient	Coefficient	Ratio	Exponent		
V		q	σ		MSR	α	β'	γ'	β'/γ'	n	$\bar{f}_b$	L
fps		psf	fps	%		fps^2/Hz						ft
Vertical component:												
100	104	11.4	0.40	0.40	0.858	0.010	0.477	0.546	0.873	1.742	1.235	3.261
200	68	44.8	0.83	0.41	0.843	0.025	0.475	0.464	1.026	1.817	1.491	3.710
200	200	44.5	0.84	0.42	0.841	0.027	0.484	0.477	1.015	1.806	1.461	3.819
250	81	69.4	1.01	0.40	0.825	0.031	0.809	0.616	1.313	1.823	1.504	3.793
300	94	98.7	0.56	0.19	0.771	0.007	0.521	0.497	1.049	1.796	1.463	3.391
350	115	131.2	1.73	0.49	0.806	0.083	0.196	0.298	0.659	1.795	1.409	4.854
400	128	167.6	1.98	0.50	0.776	0.082	0.667	0.533	1.252	1.835	1.567	4.163
450	141	207.3	3.46	0.77	0.813	0.264	0.397	0.349	1.138	1.923	1.815	4.948
500	154	248.8	3.33	0.67	0.731	0.200	0.875	0.688	1.271	1.777	1.406	4.504
500	173	248.5	2.85	0.57	0.712	0.124	0.687	0.560	1.227	1.810	1.516	3.796
500	196	249.6	2.32	0.46	0.687	0.096	0.848	0.810	1.046	1.689	1.148	4.454
Average				0.48			0.585	0.531	1.079	1.801	1.456	4.063
Lateral component:												
100	218	11.2	0.41	0.41	0.861	0.012	0.657	0.672	0.978	1.734	1.202	3.558
150	217	25.3	0.60	0.40	0.853	0.017	0.461	0.488	0.945	1.784	1.381	3.567
200	216	45.0	0.84	0.42	0.834	0.025	0.436	0.455	0.956	1.801	1.441	3.643
250	215	69.8	1.02	0.41	0.825	0.031	0.348	0.378	0.919	1.833	1.545	3.734
300	214	99.9	0.98	0.33	0.789	0.024	0.403	0.430	0.938	1.802	1.466	3.769
350	213	135.2	1.53	0.44	0.772	0.056	0.370	0.425	0.869	1.778	1.401	4.177
400	212	175.5	1.39	0.35	0.624	0.025	1.130	1.042	1.084	1.657	1.042	2.557
450	205	207.1	2.09	0.46	0.759	0.076	1.113	0.711	1.565	1.842	1.546	3.940
450	211	221.1	2.35	0.52	0.737	0.100	0.682	0.713	0.956	1.747	1.149	4.070
500	204	251.4	3.05	0.61	0.802	0.176	0.502	0.382	1.313	1.955	1.866	4.720
Average				0.43			0.610	0.570	1.052	1.793	1.404	3.774

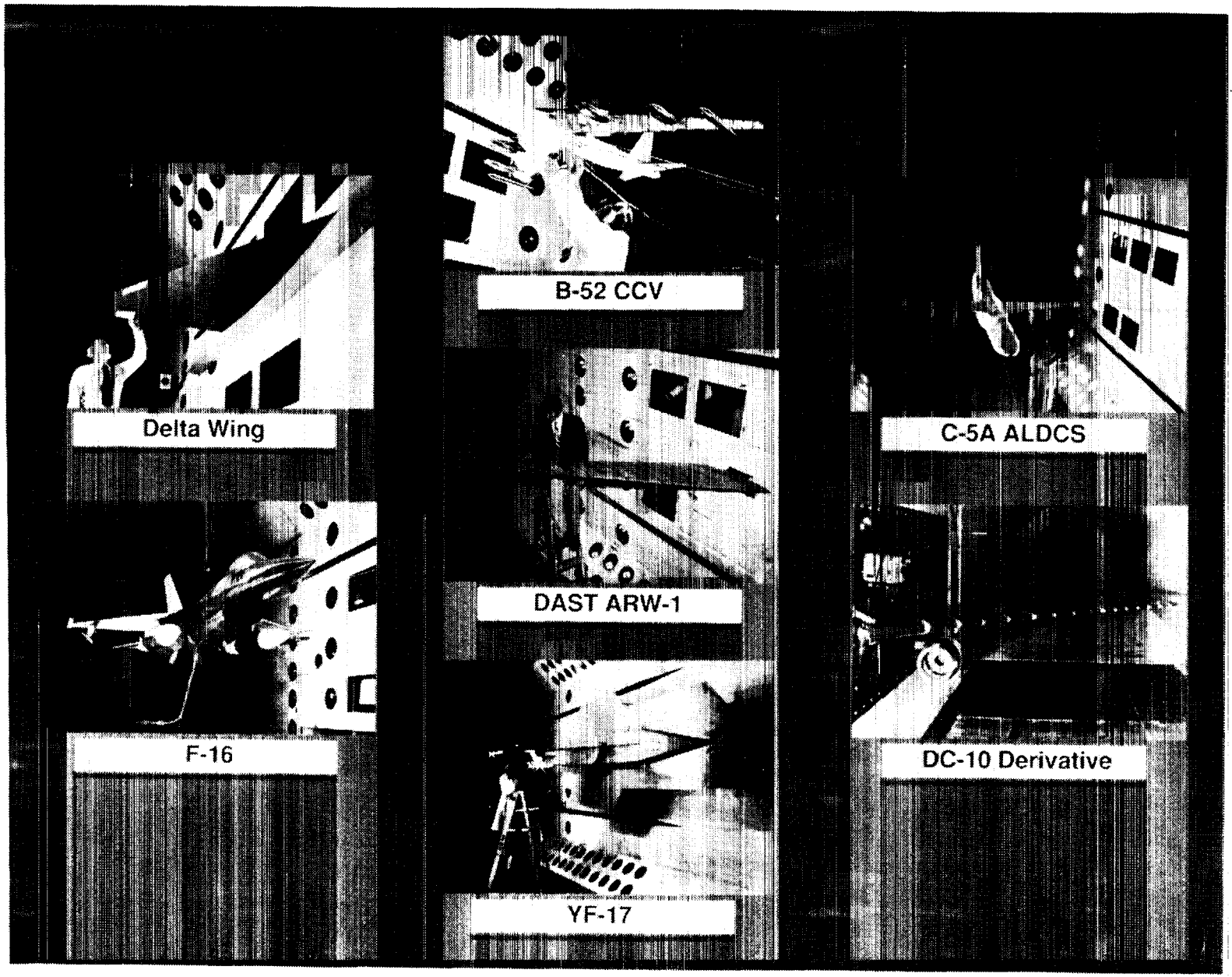

Figure 1. Active control wind-tunnel studies.

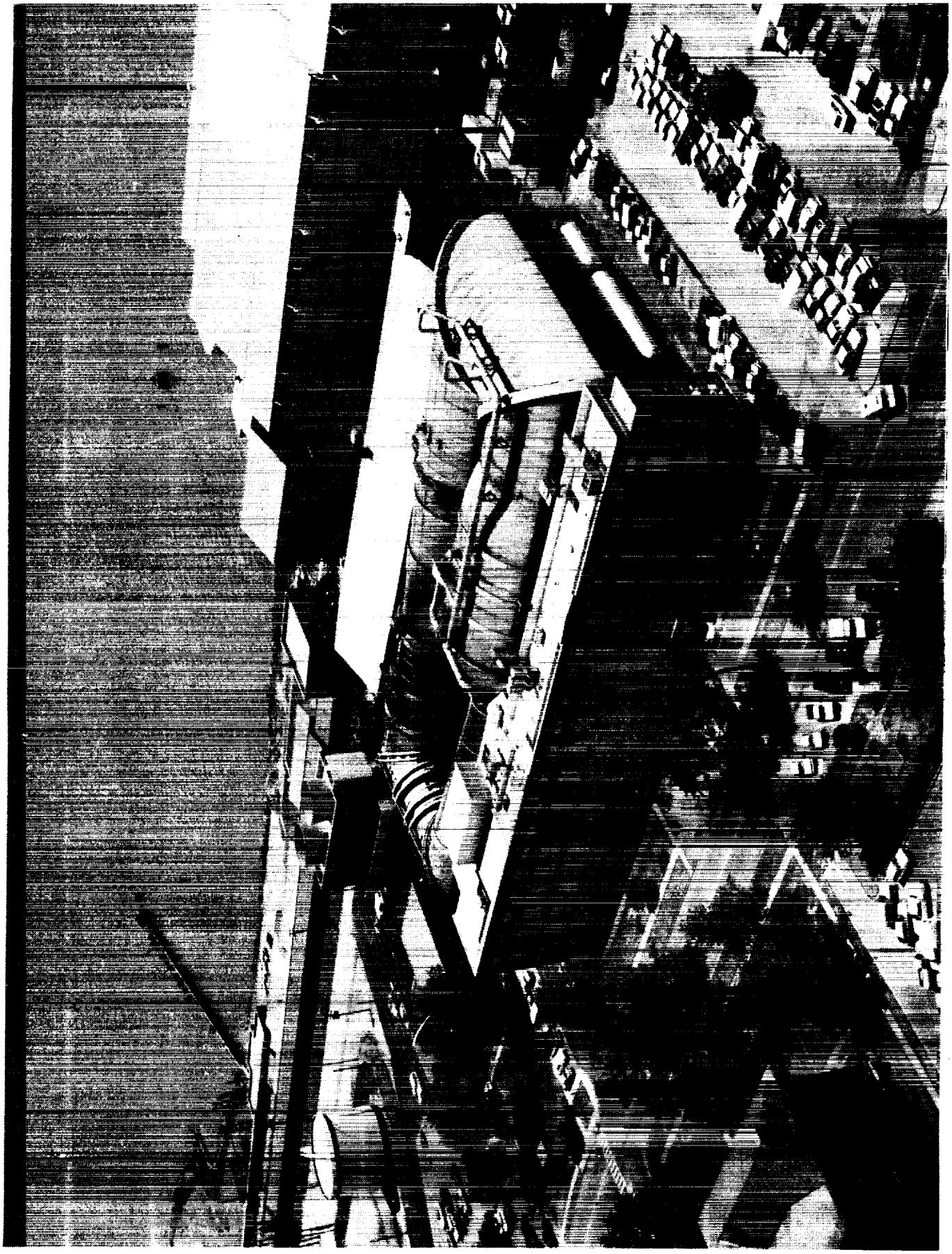

Figure 2. Aerial view of the Langley Transonic Dynamics Tunnel facility.

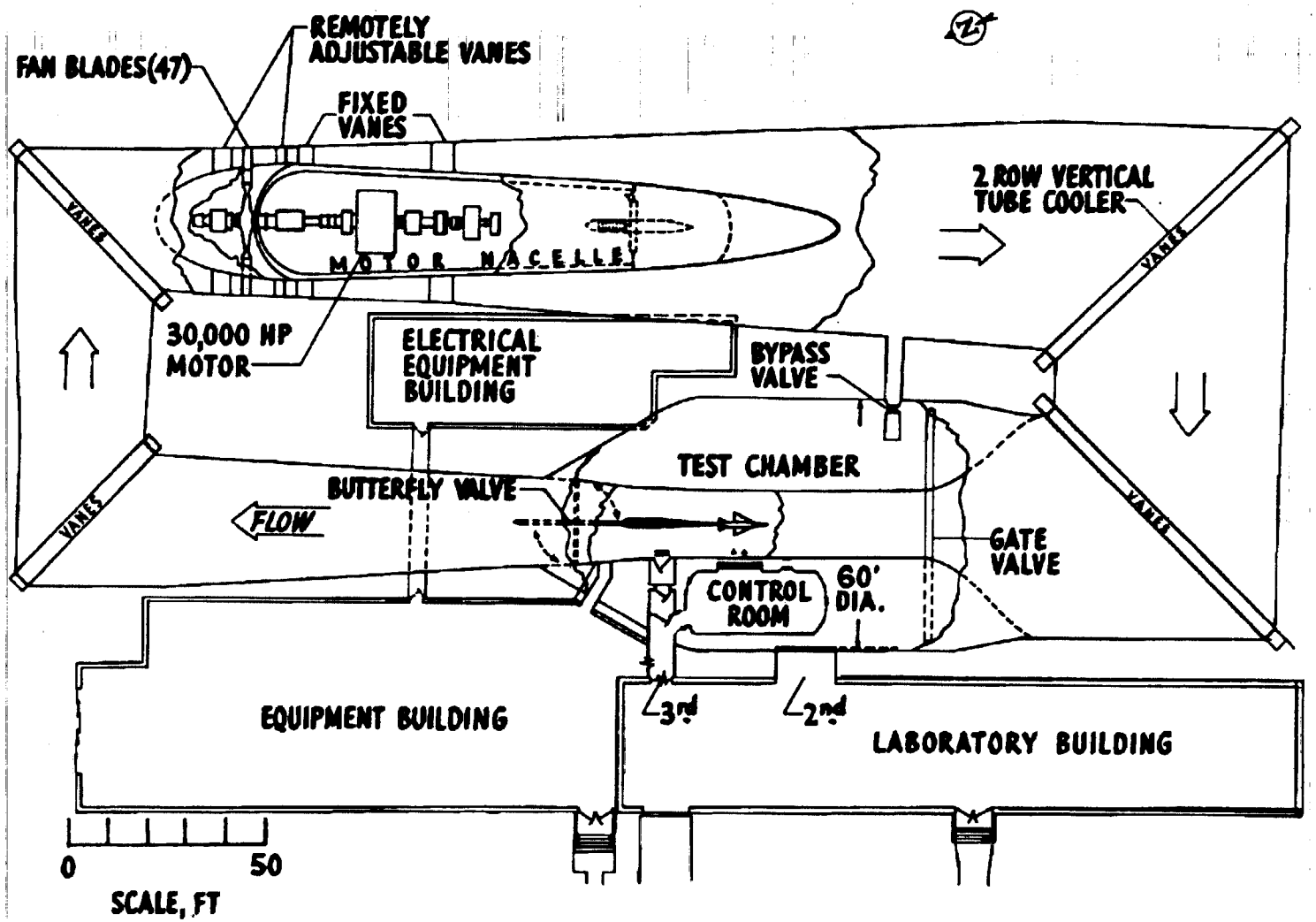

Figure 3. Plan view of the Langley Transonic Dynamics Tunnel facility.

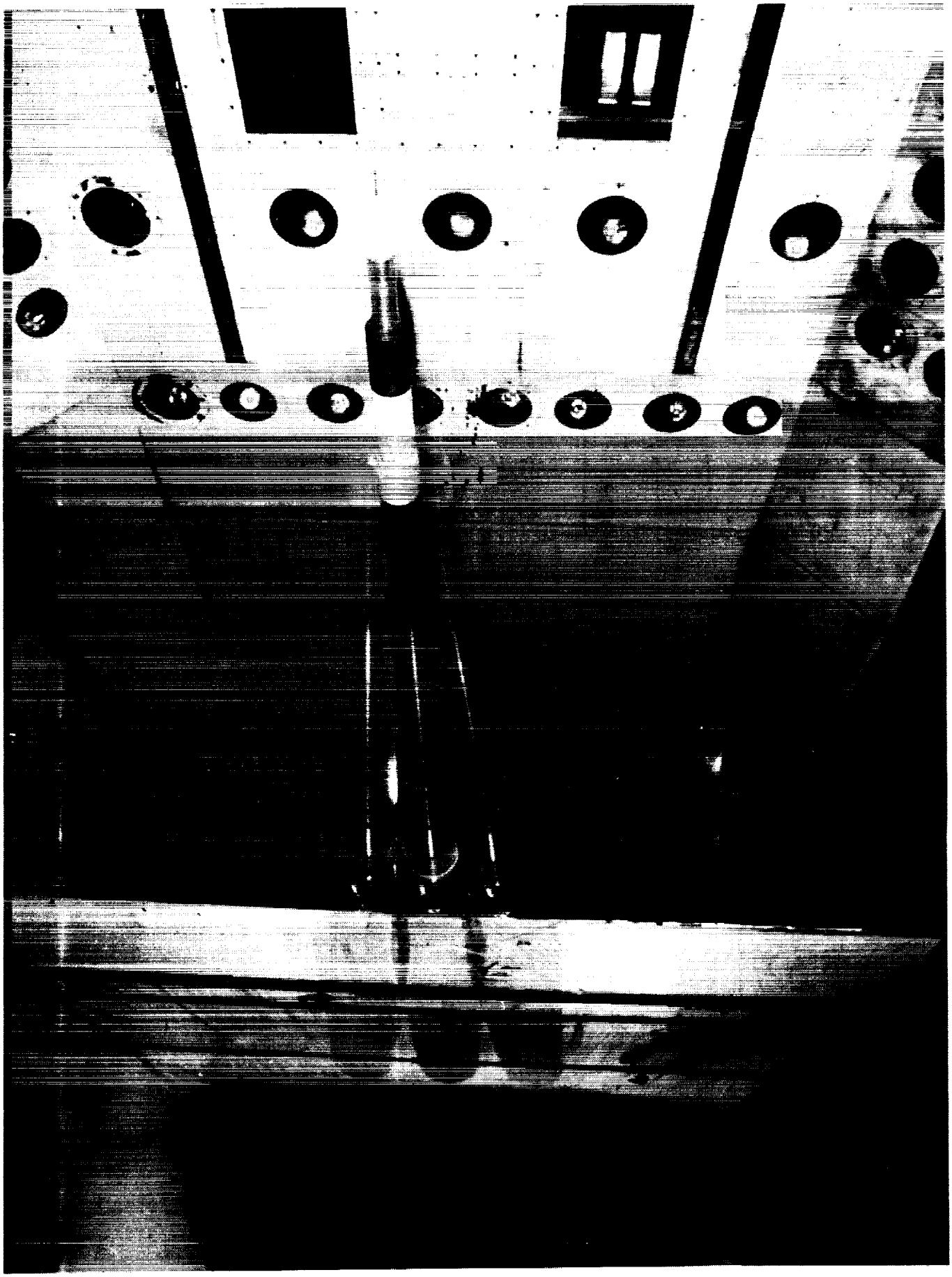

Figure 4. Wind tunnel test section showing range of sting pitch positions.

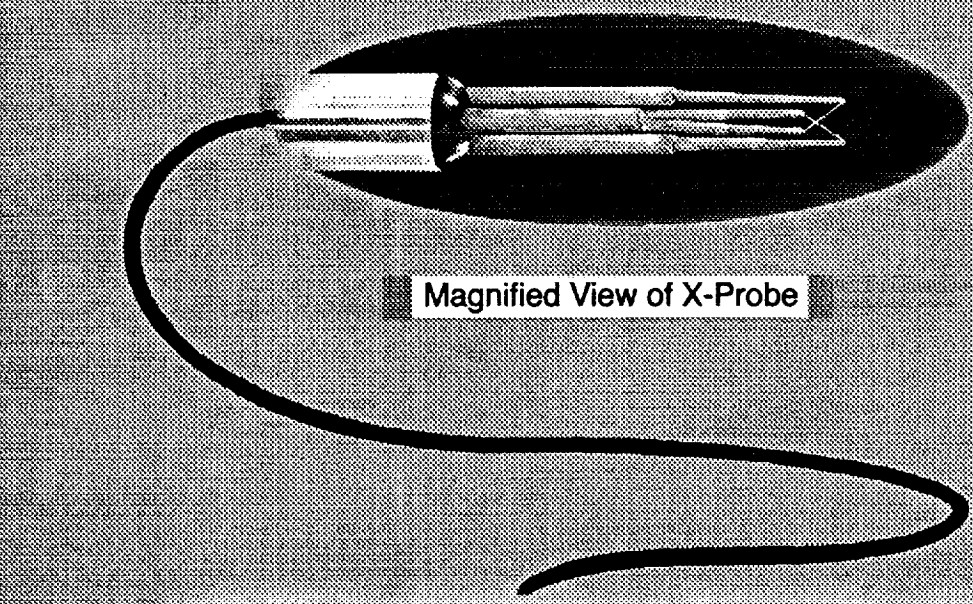

Magnified View of X-Probe

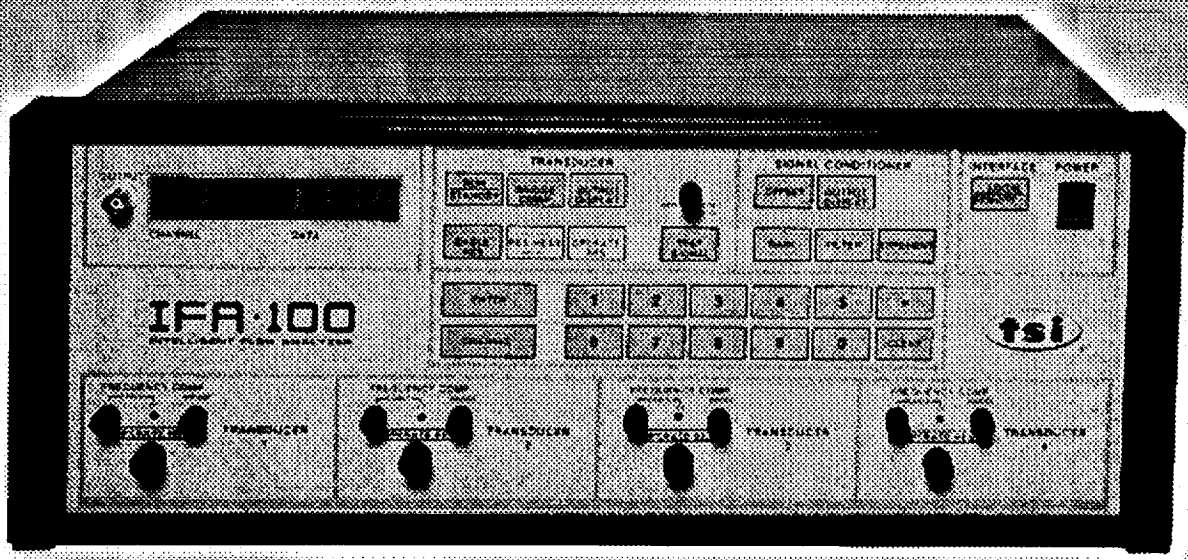

Anemometer Console

Figure 5. Anemometry system.

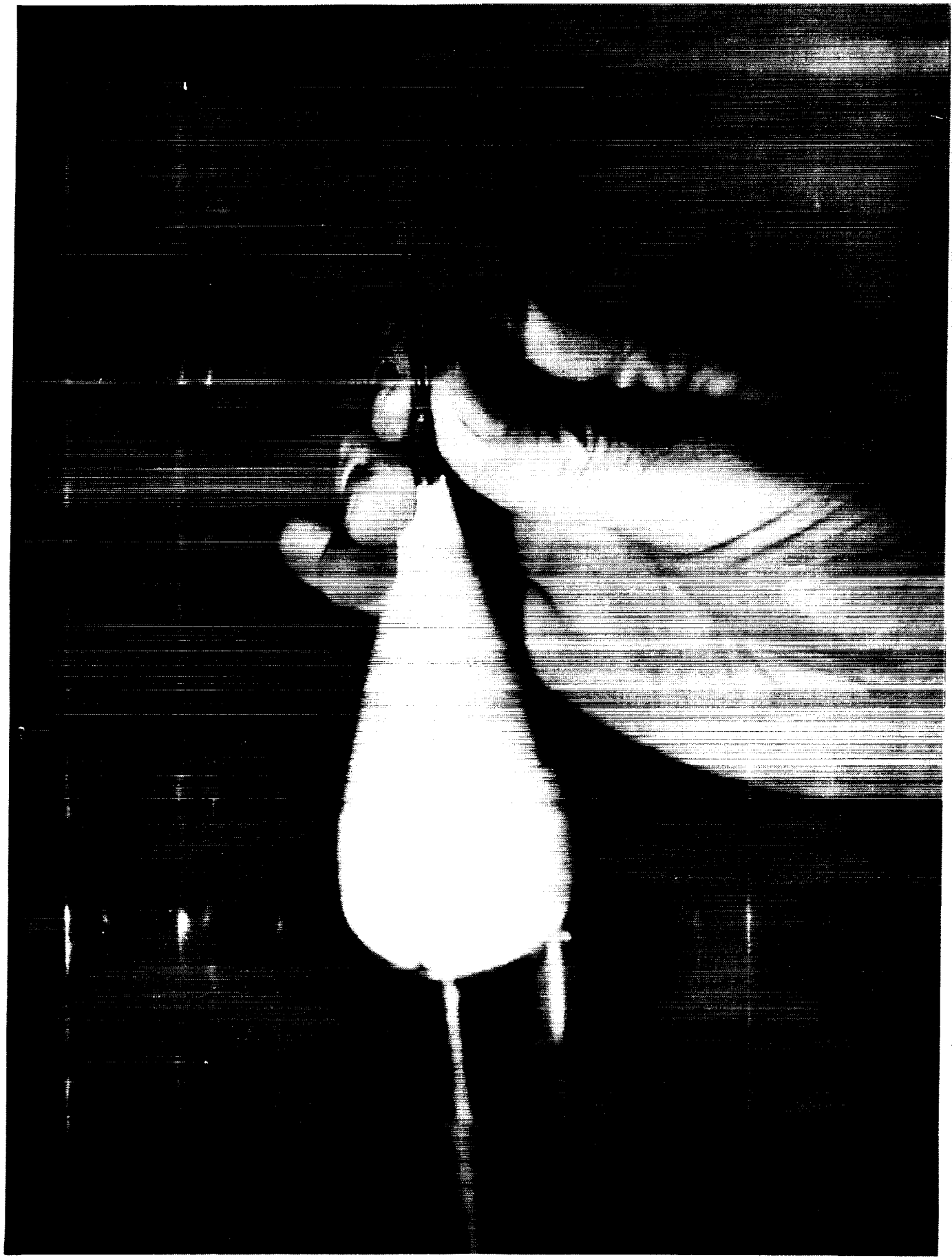

Figure 6. View of X-probe. Actual size.

Figure 7. Probe installation at tip of sting in test section.

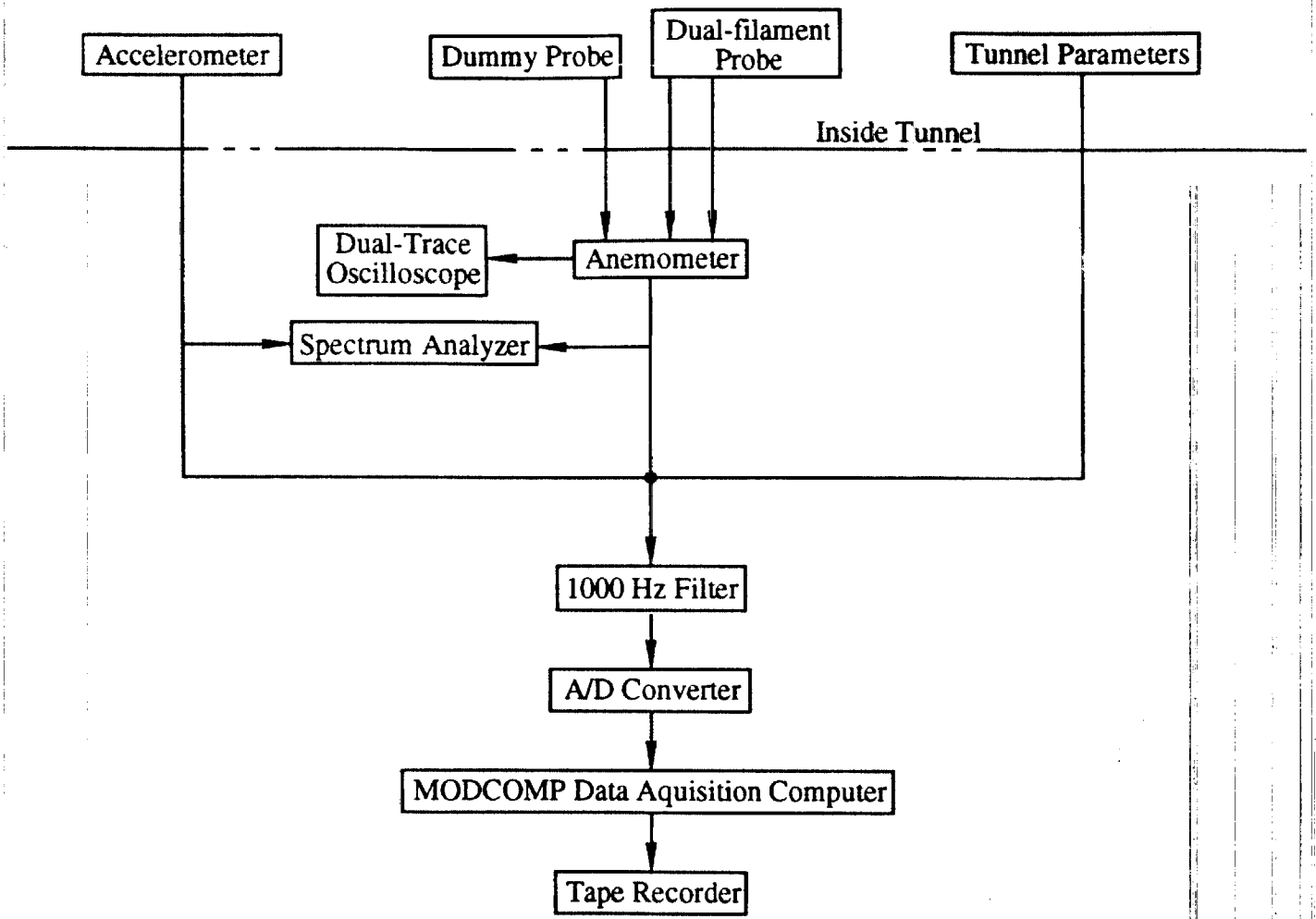

Figure 8. Data acquisition system block diagram

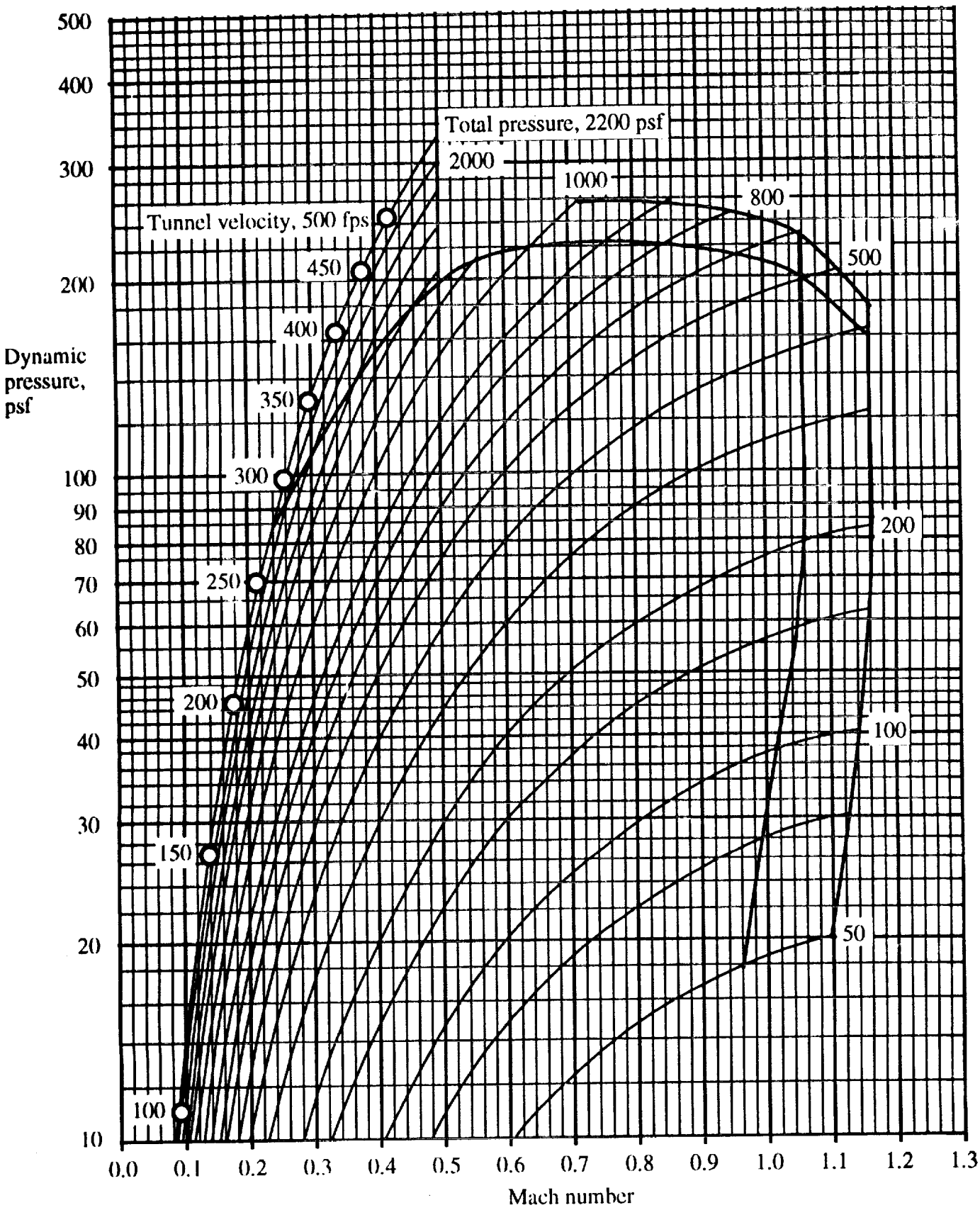

Figure 9. Transonic Dynamics Tunnel operating boundary in air. Open circles denote test conditions.

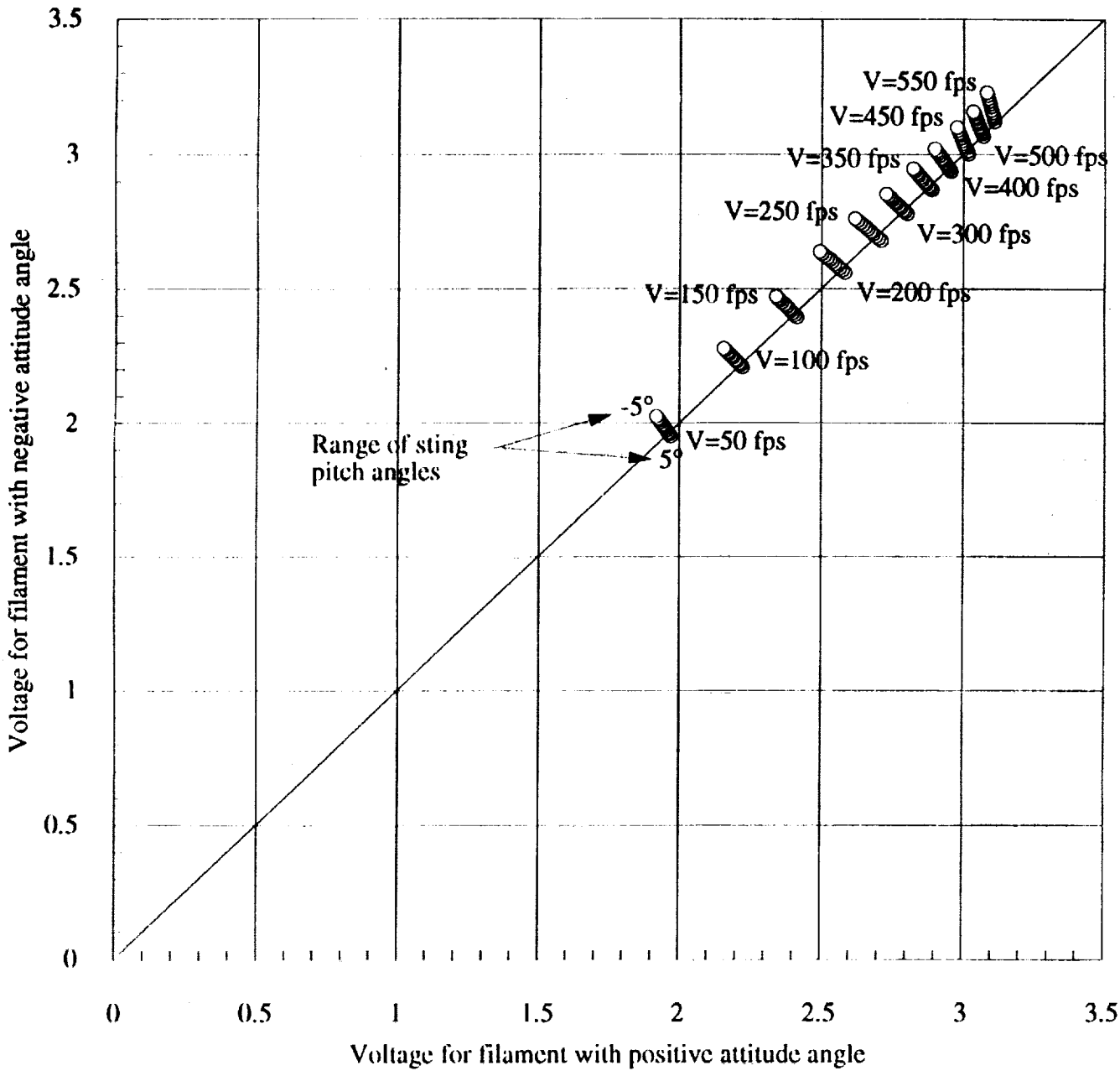

Figure 10. X-probe calibration voltage grid.

This page left blank intentionally.

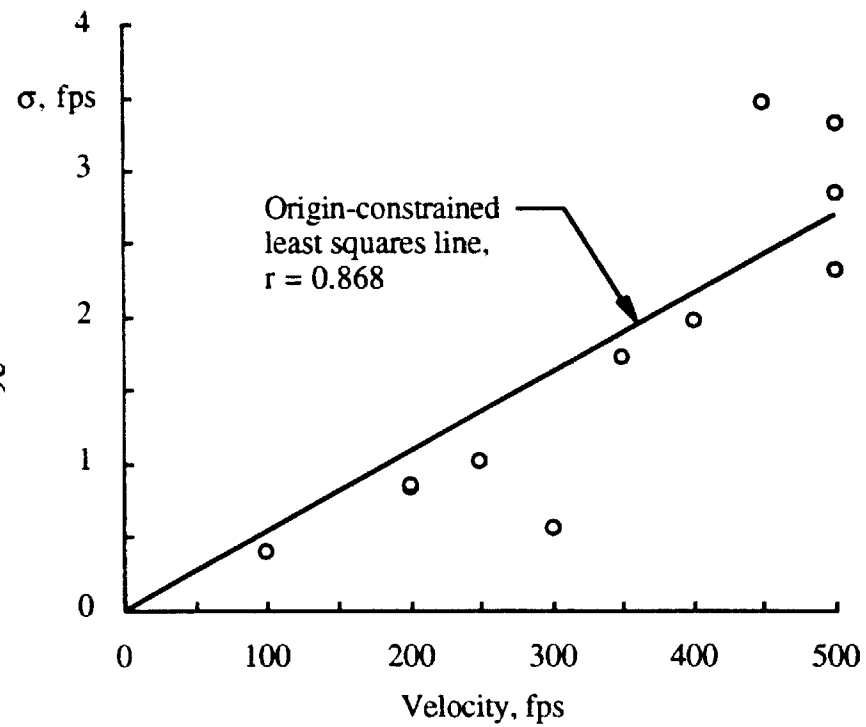

(a) With tunnel velocity.

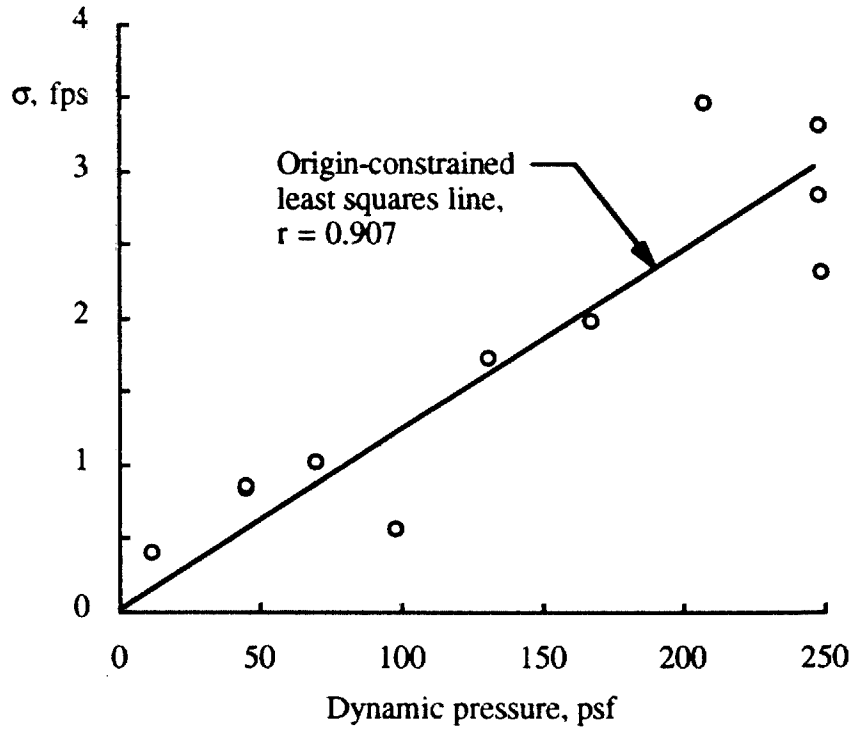

(b) With dynamic pressure.

Figure 11. Variation of standard deviation of the vertical component of tunnel turbulence.

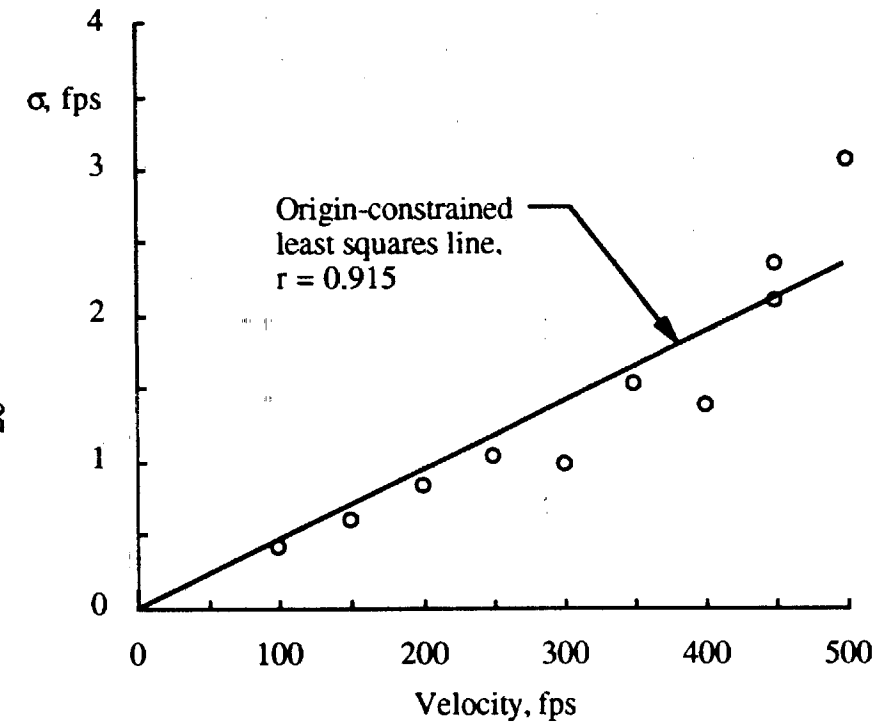

(a) With tunnel velocity.

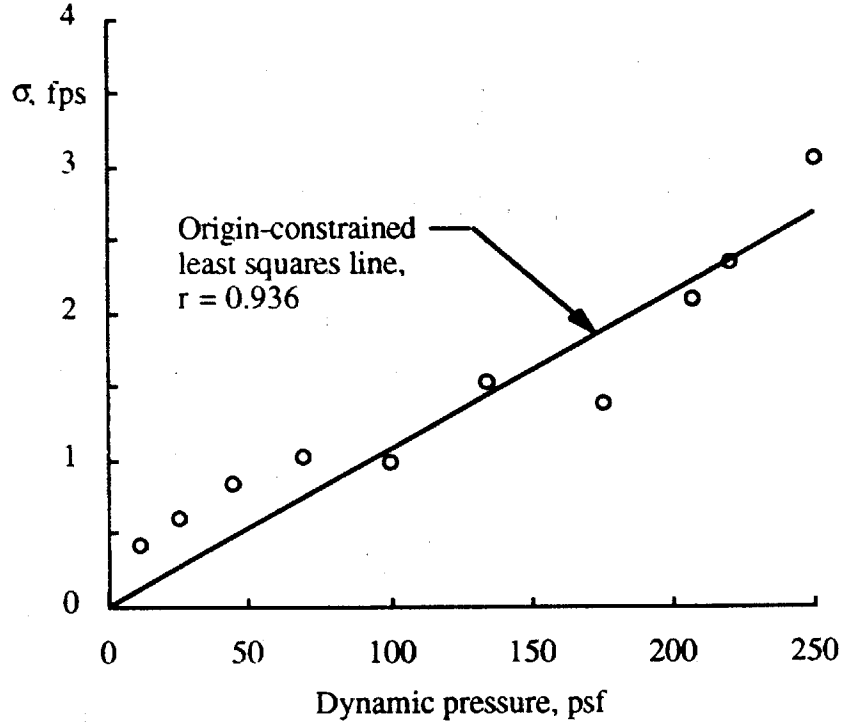

(b) With dynamic pressure.

Figure 12. Variation of standard deviation of the lateral component of tunnel turbulence.

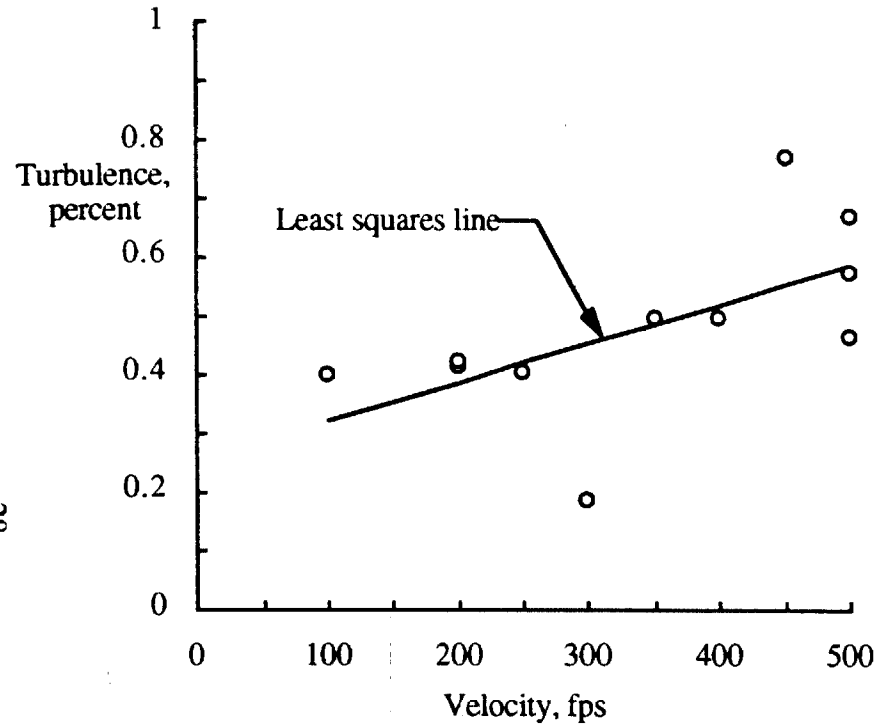

(a) With tunnel velocity.

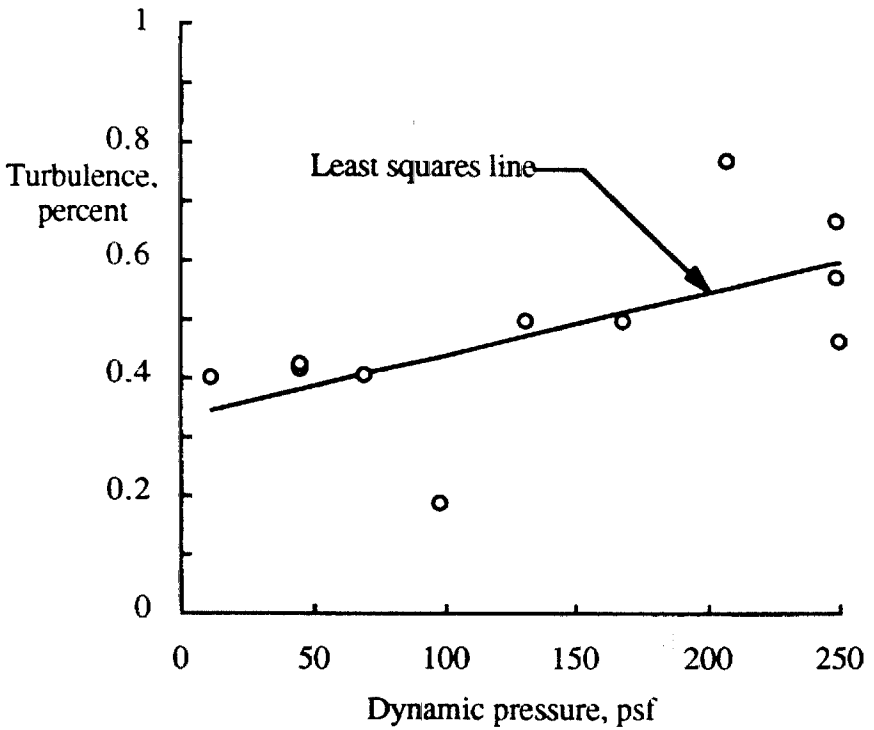

(b) With dynamic pressure.

Figure 13. Variation of vertical component of turbulence.

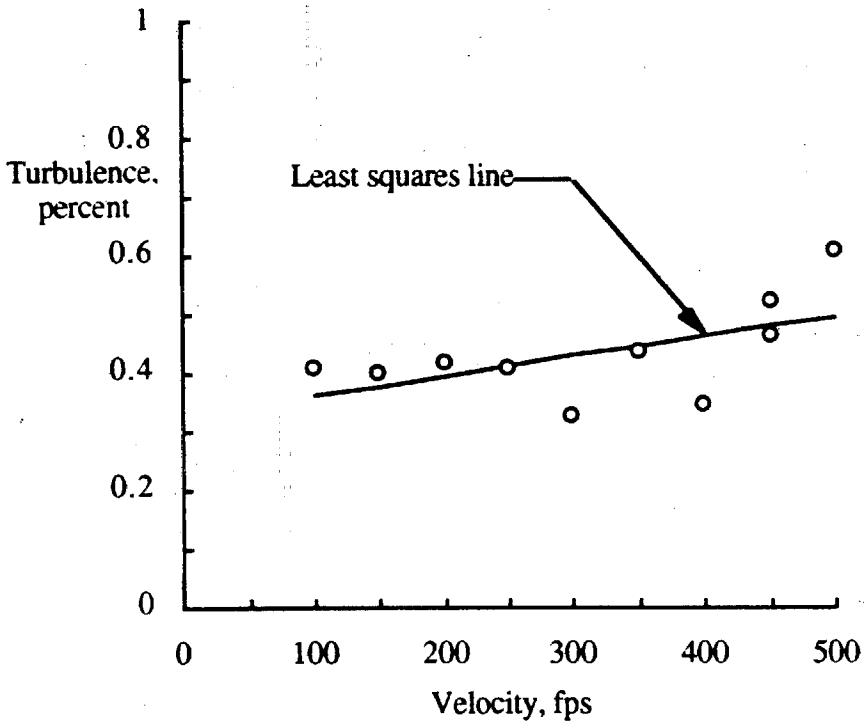

(a) With tunnel velocity.

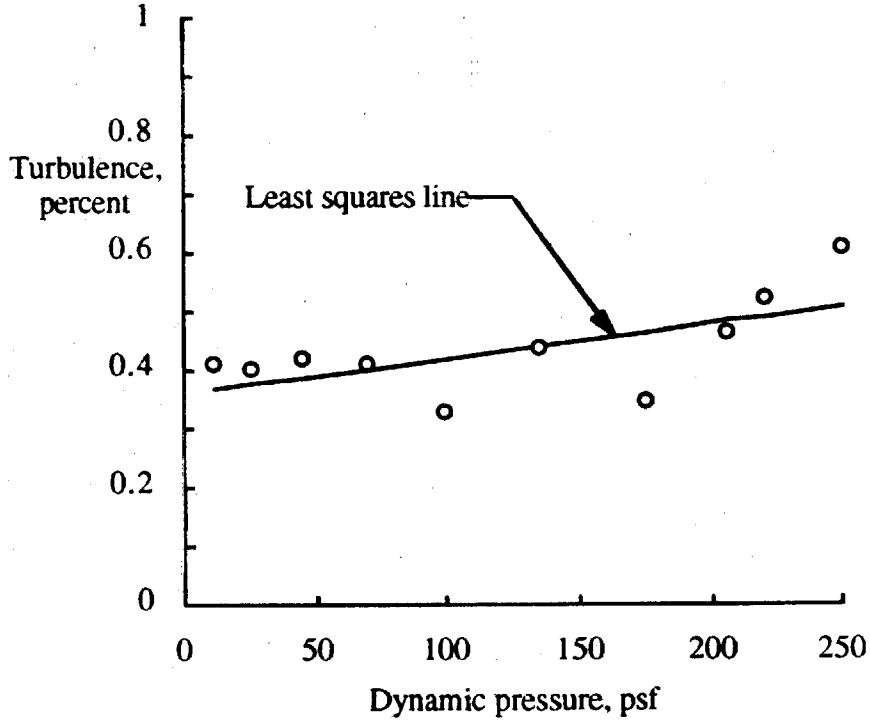

(b) With dynamic pressure.

Figure 14. Variation of lateral component of turbulence.

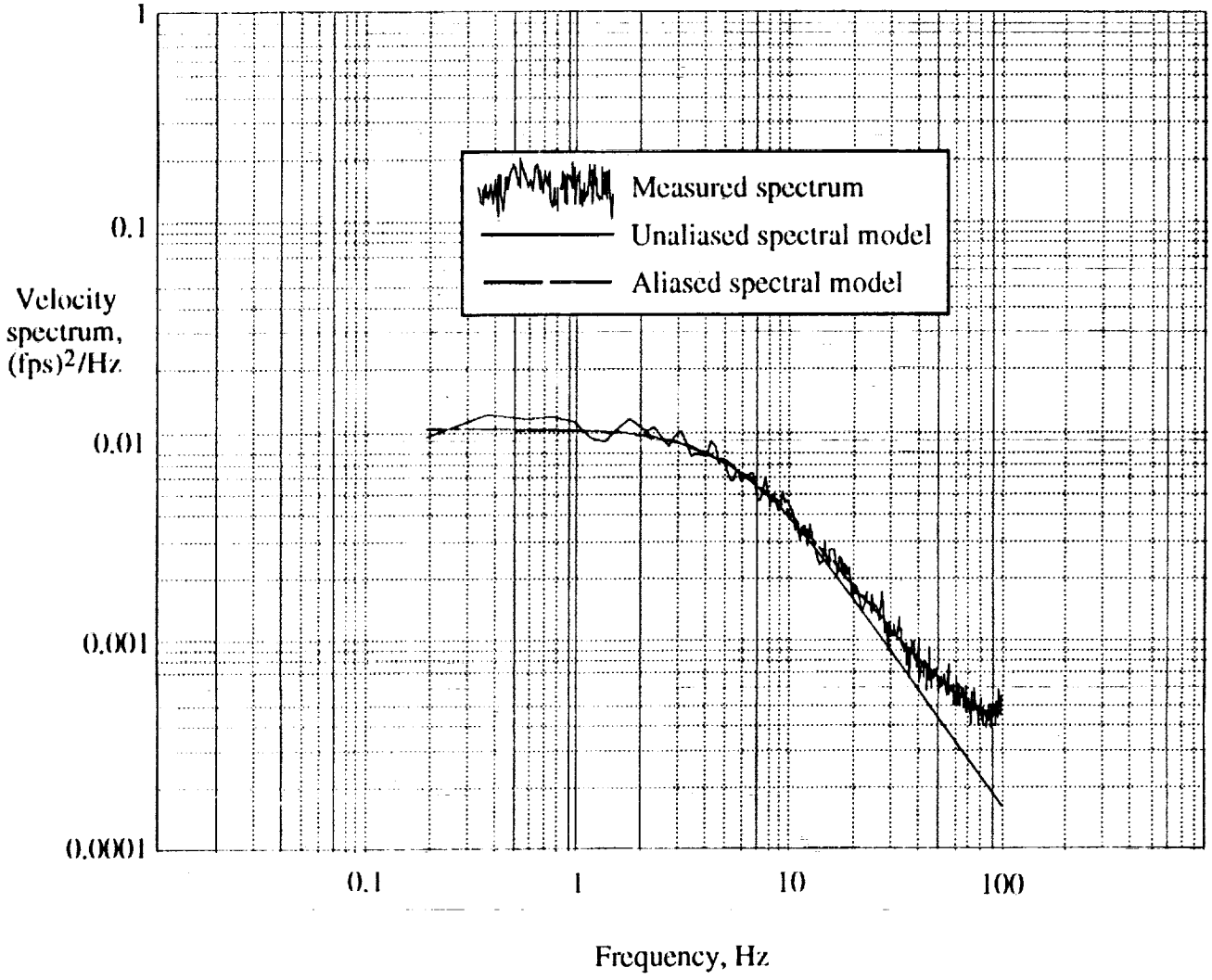

(a) Tunnel velocity 100 fps (tab point 104).

Figure 15. Power spectral density functions of vertical component of tunnel turbulence.

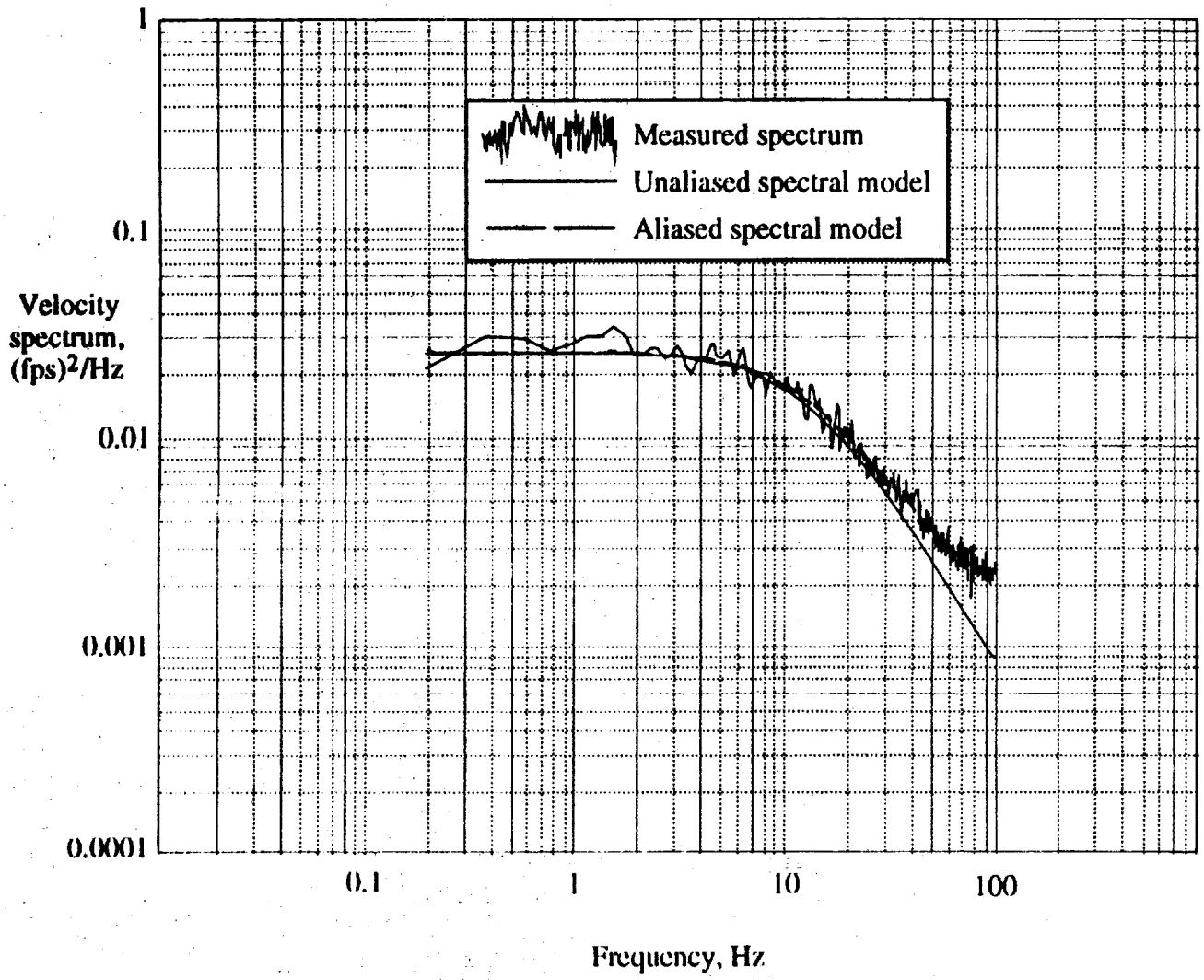

(b) Tunnel velocity 200 fps (tab point 68).

Figure 15. Continued.

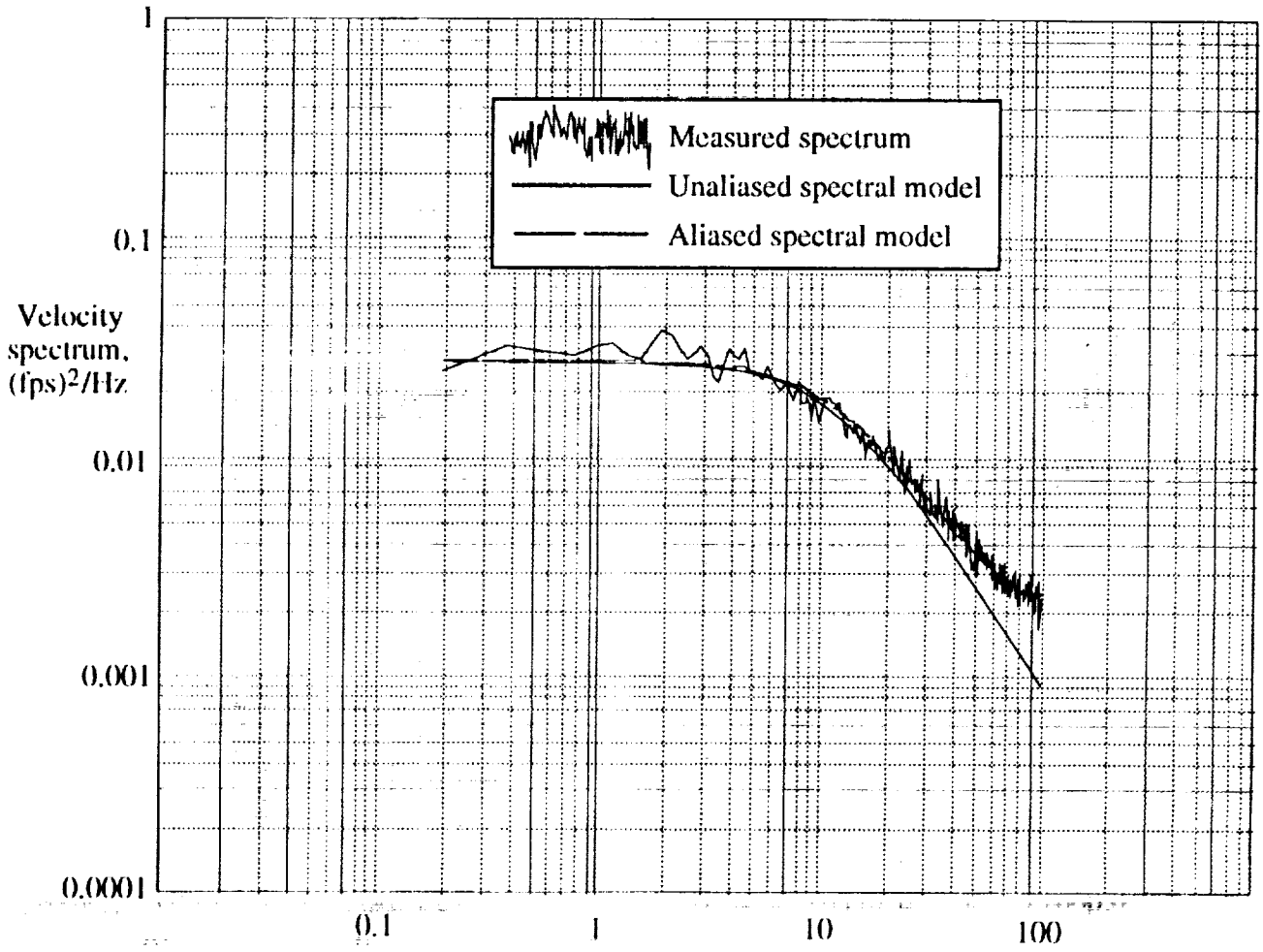

(c) Tunnel velocity 200 fps (tab point 200).

Figure 15. Continued.

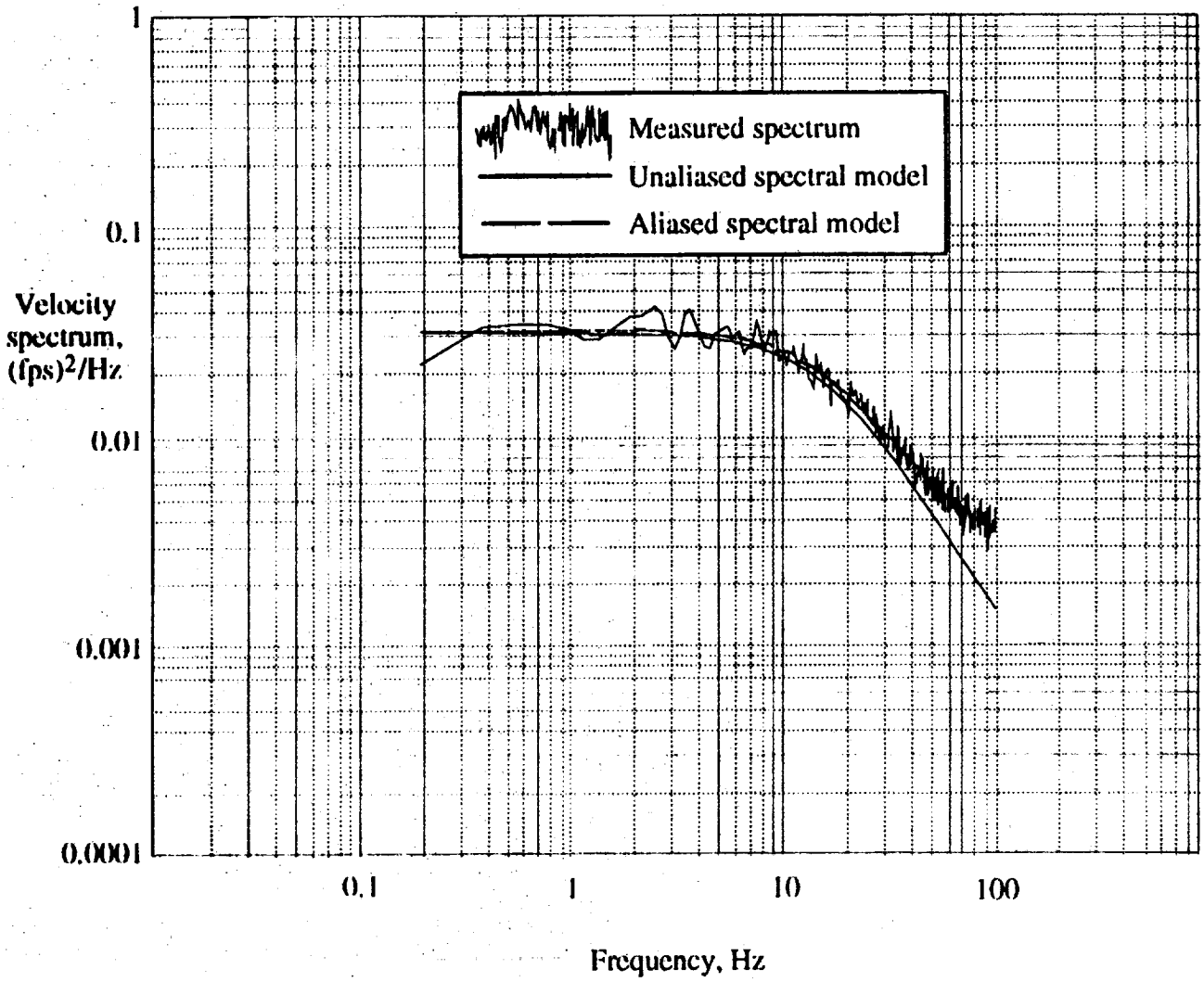

(d) Tunnel velocity 250 fps (tab point 81).

Figure 15. Continued.

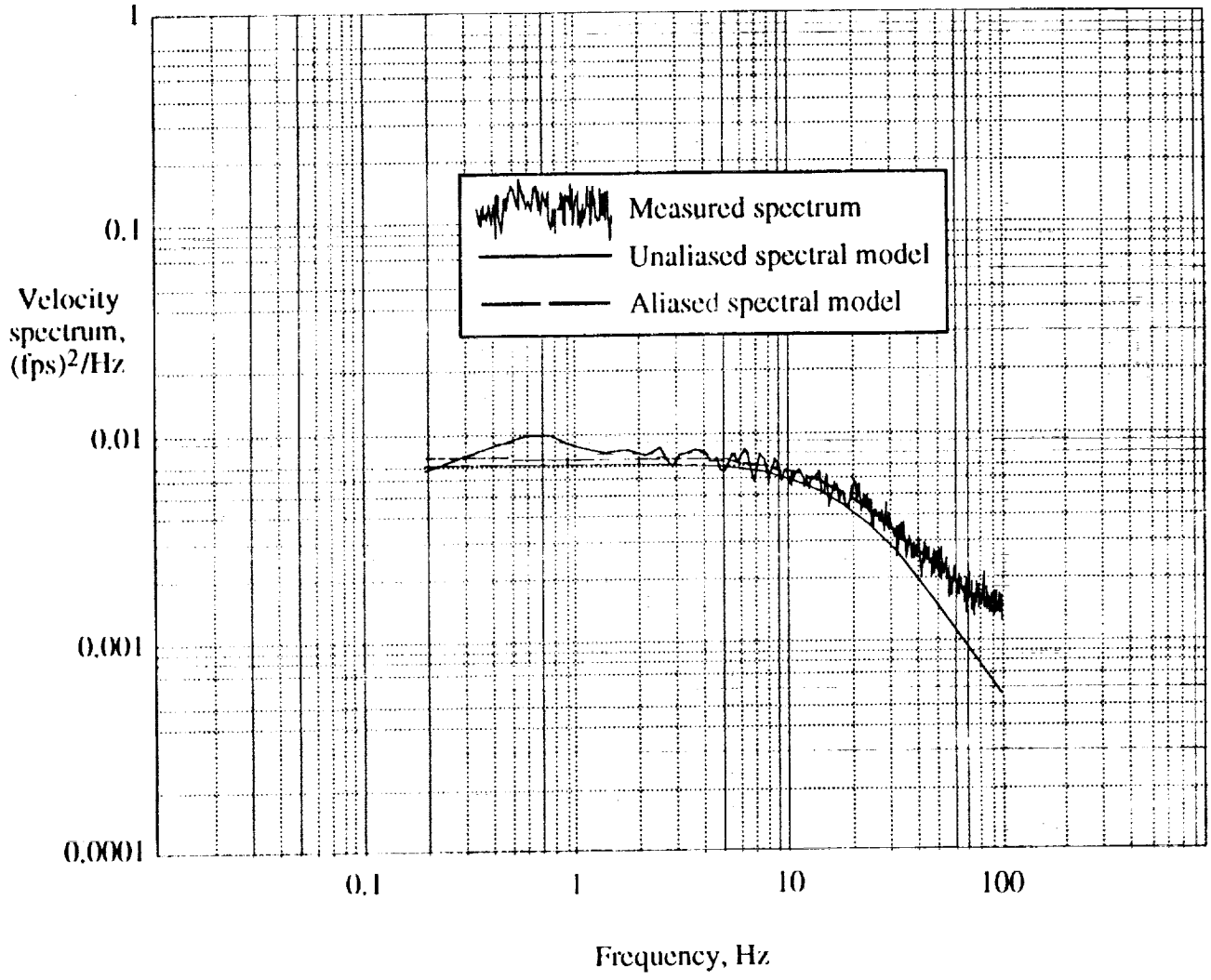

(e) Tunnel velocity 300 fps (tab point 94).

Figure 15. Continued.

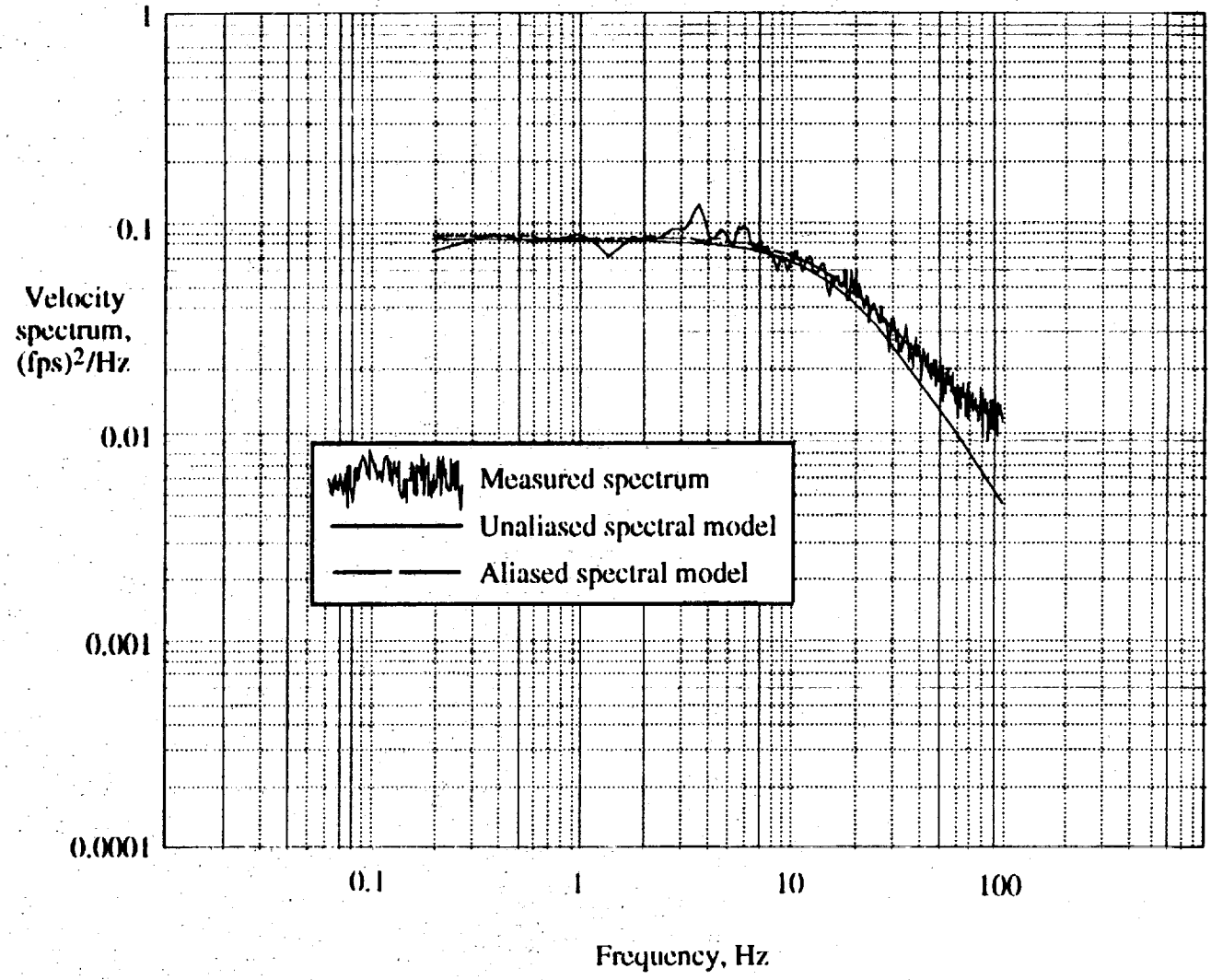

(f) Tunnel velocity 350 fps (tab point 115).

Figure 15. Continued.

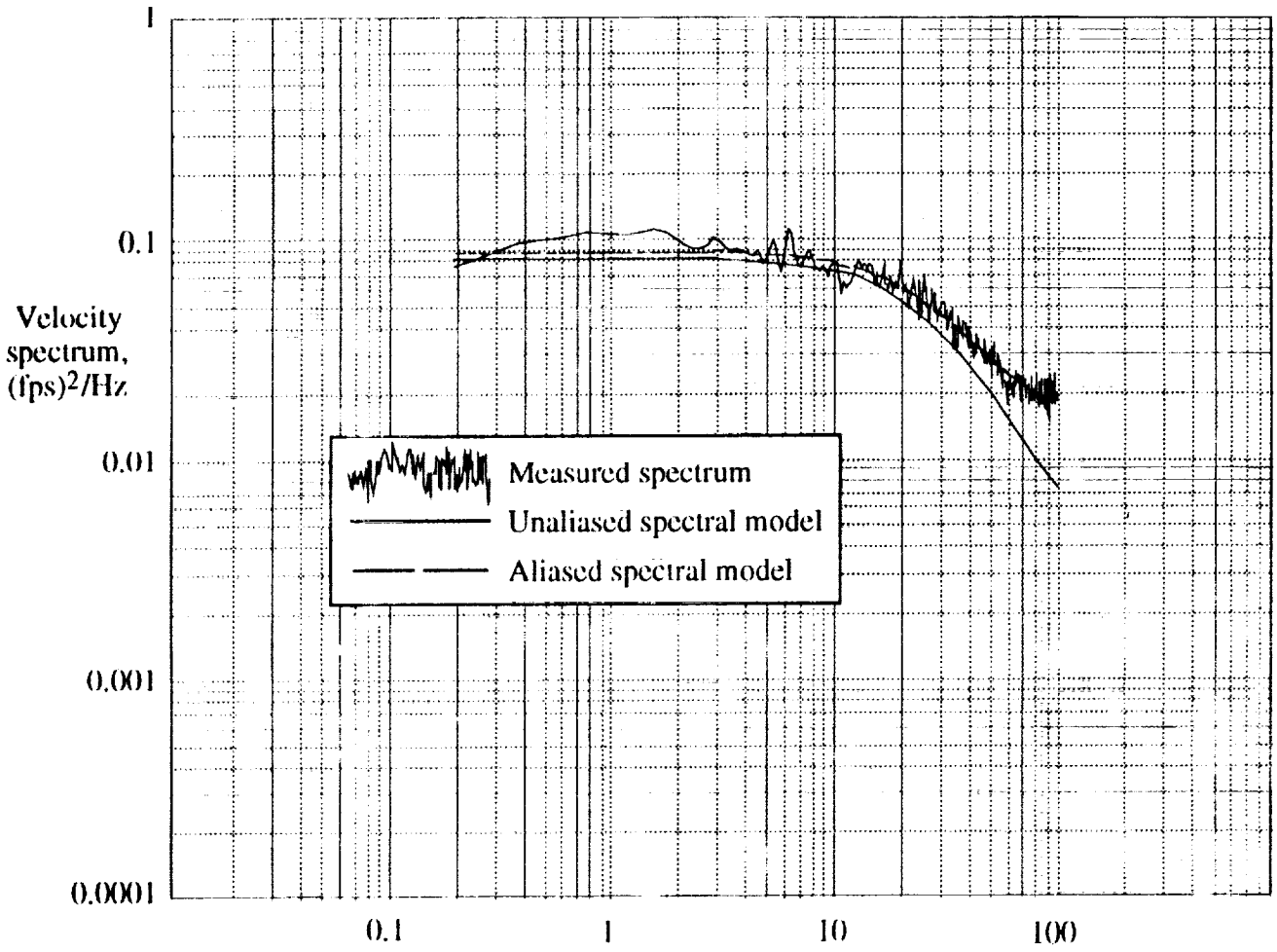

(g) Tunnel velocity 400 fps (tab point 128).

Figure 15. Continued.

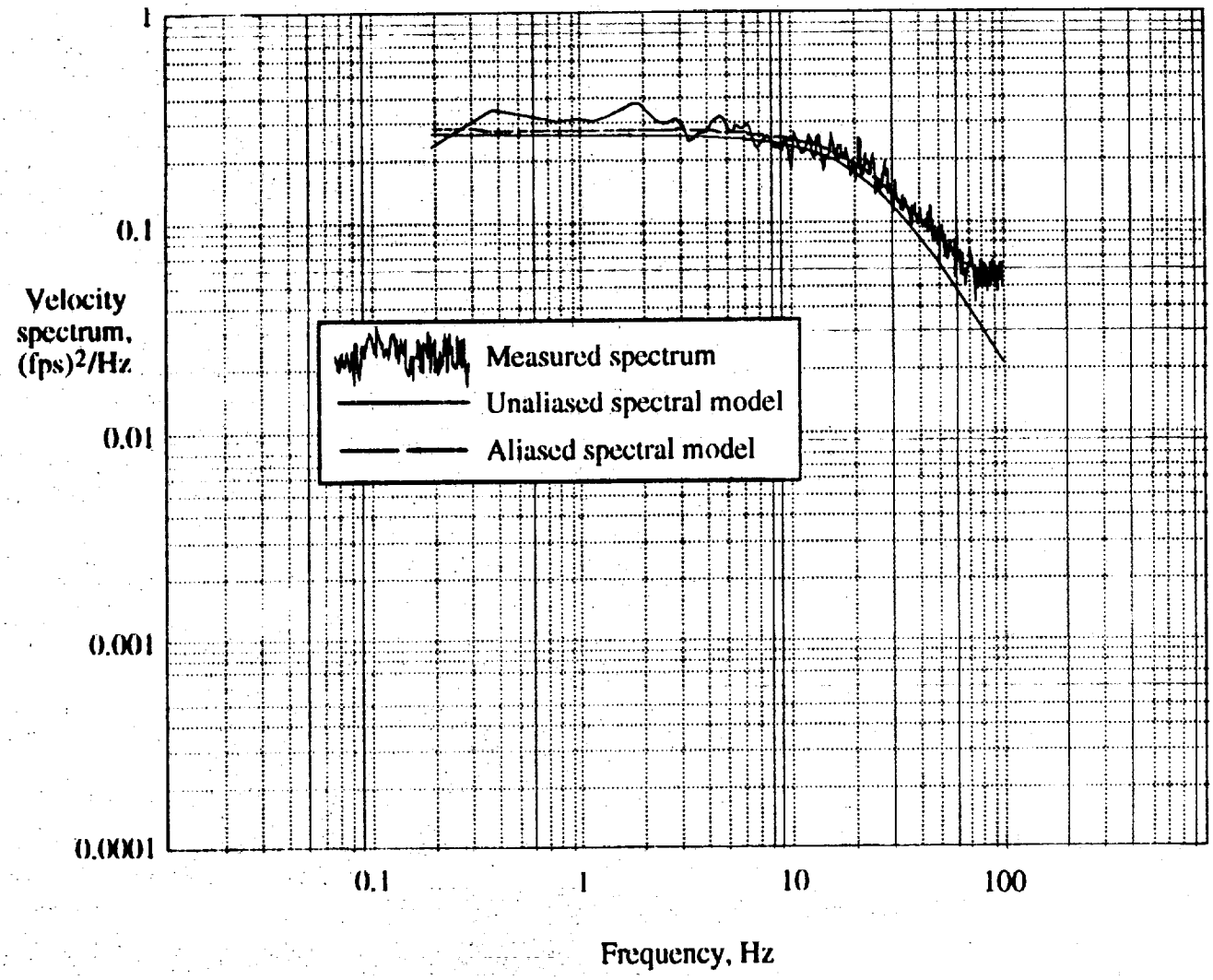

(h) Tunnel velocity 450 fps (tab point 141).

Figure 15. Continued.

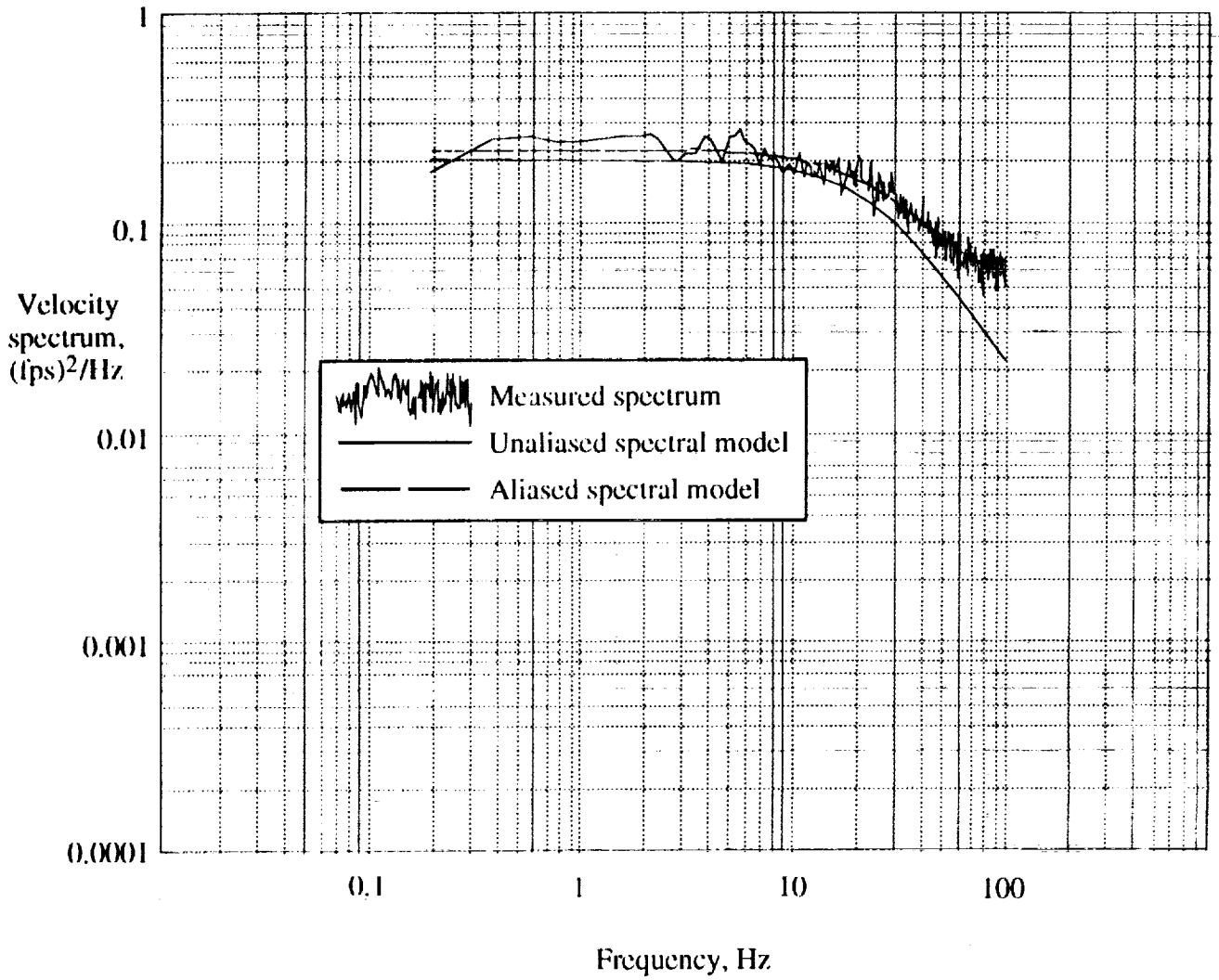

(i) Tunnel velocity 500 fps (tab point 154).

Figure 15. Continued.

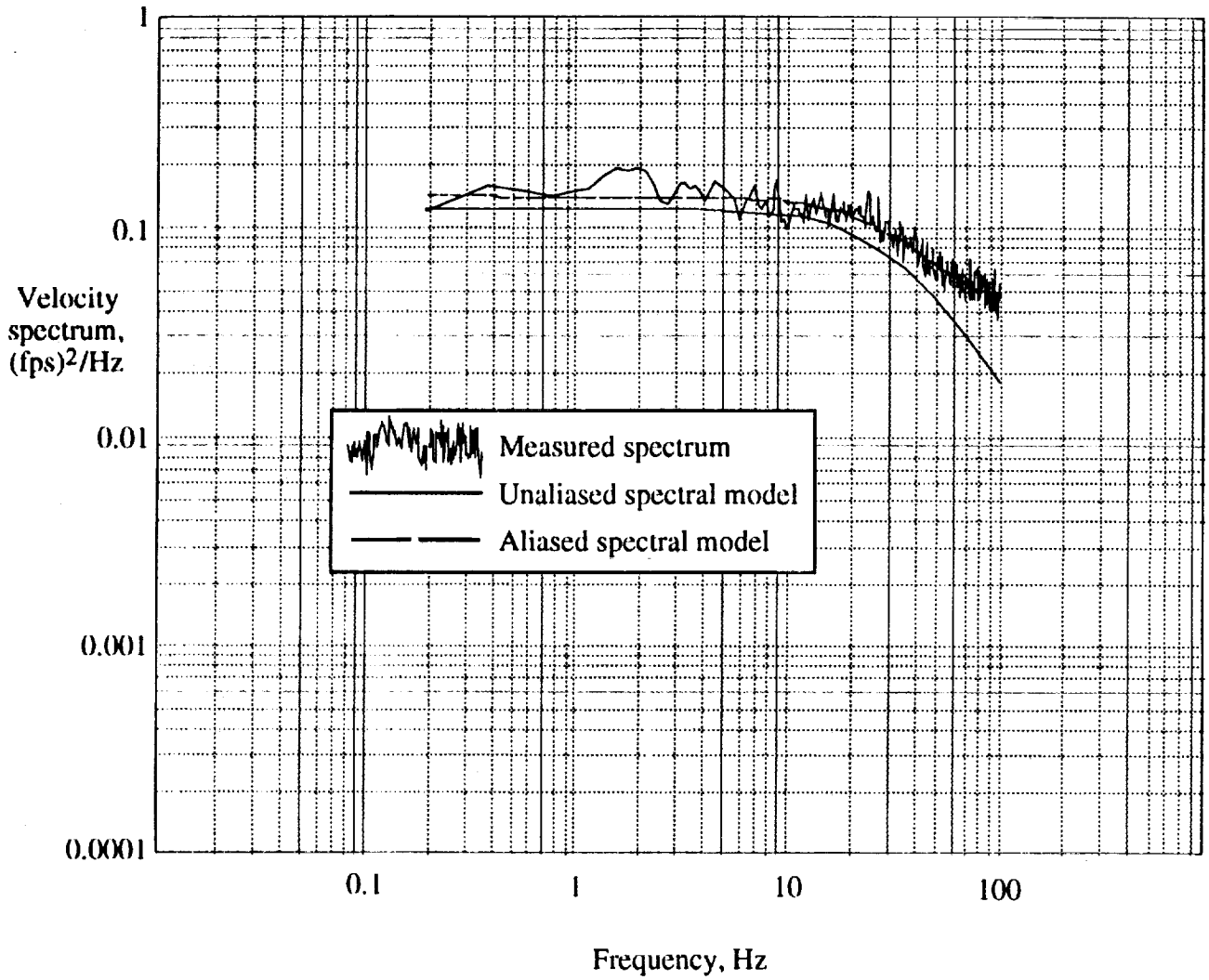

(j) Tunnel velocity 500 fps (tab point 173).

Figure 15. Continued.

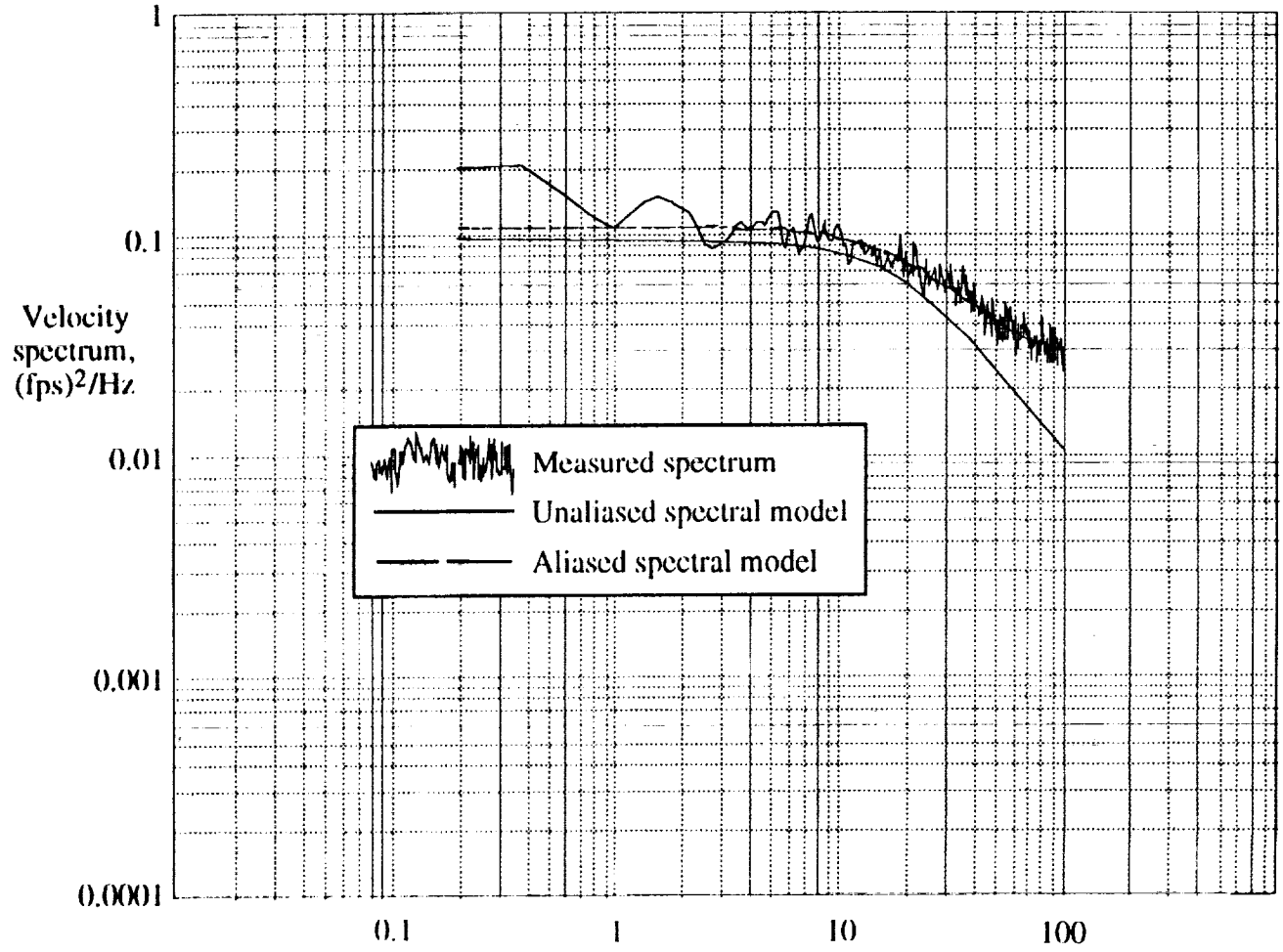

(k) Tunnel velocity 500 fps (tab point 196).

Figure 15. Concluded.

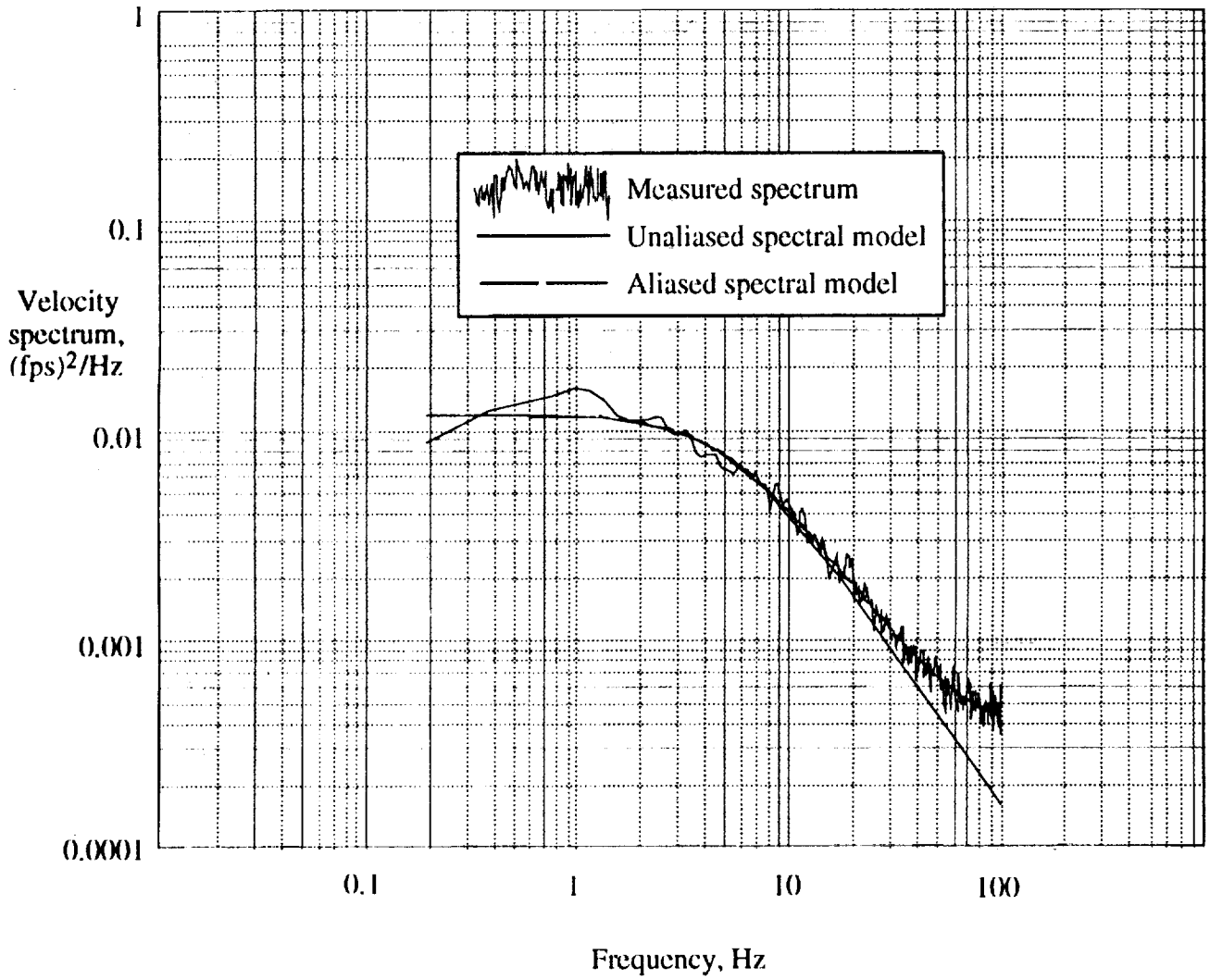

(a) Tunnel velocity 100 fps (tab point 218).

Figure 16. Power spectral density functions of lateral component of tunnel turbulence.

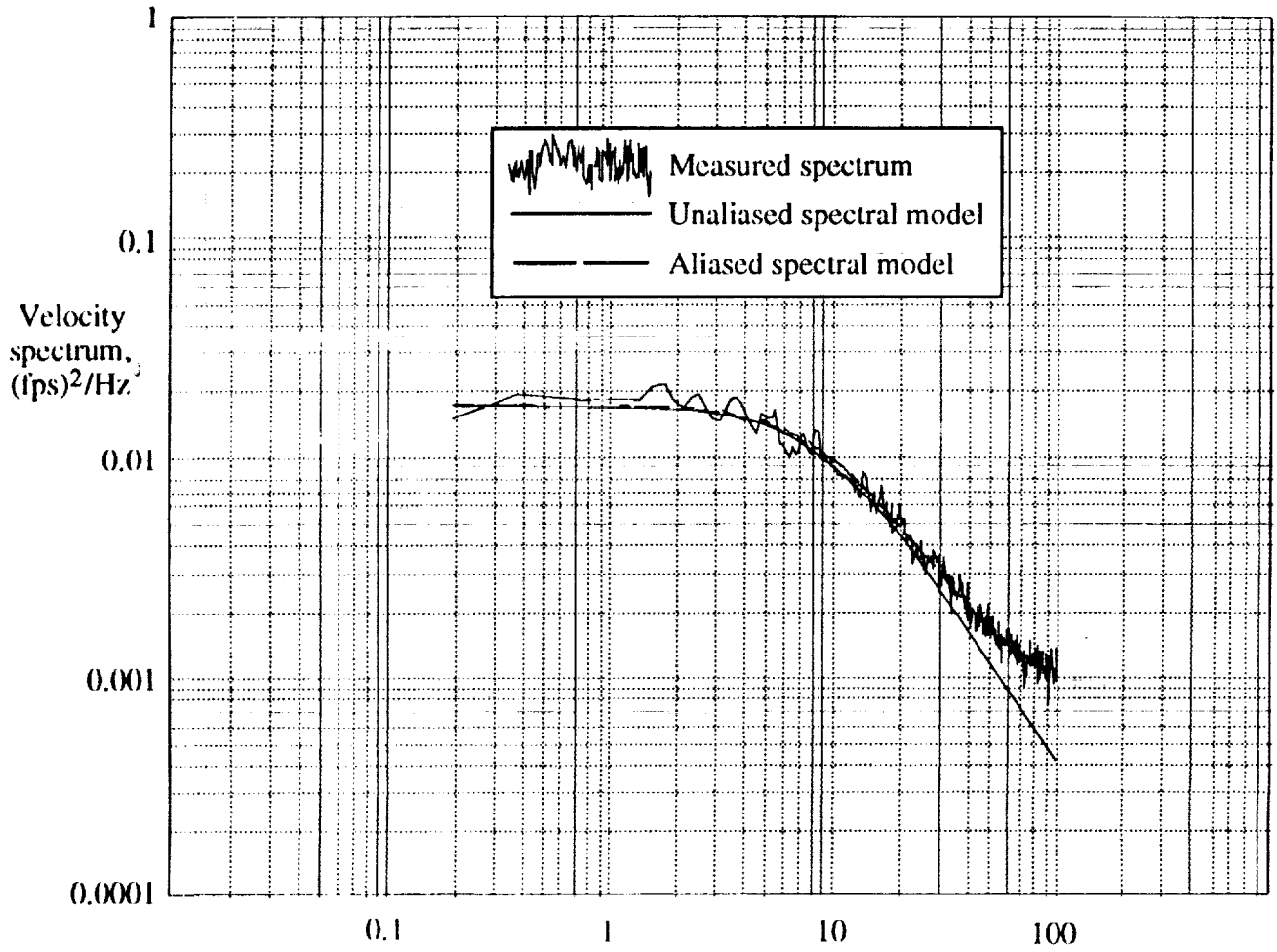

(b) Tunnel velocity 150 fps (tab point 217).

Figure 16. Continued.

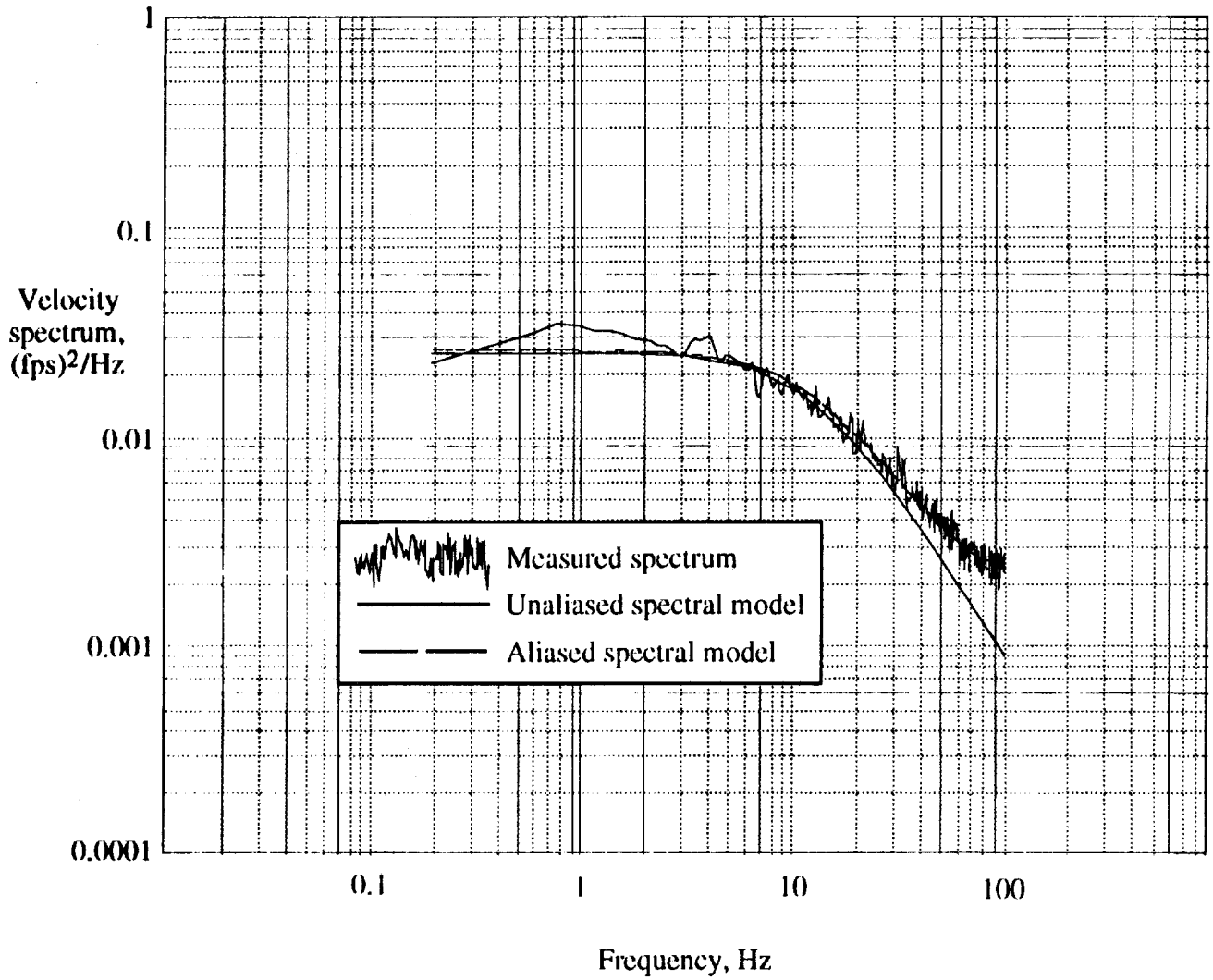

(c) Tunnel velocity 200 fps (tab point 216).

Figure 16. Continued.

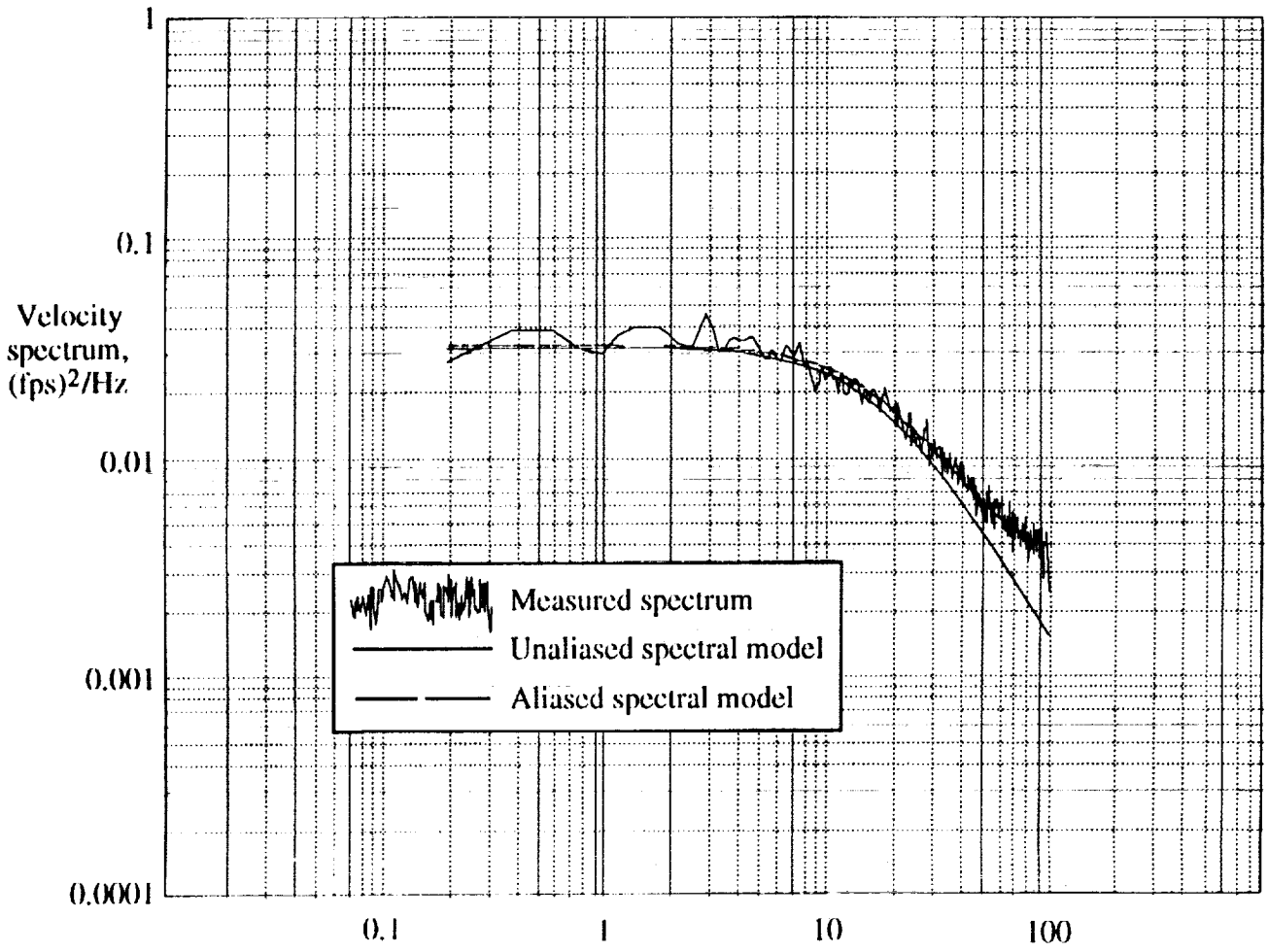

(d) Tunnel velocity 250 fps (tab point 215).

Figure 16. Continued.

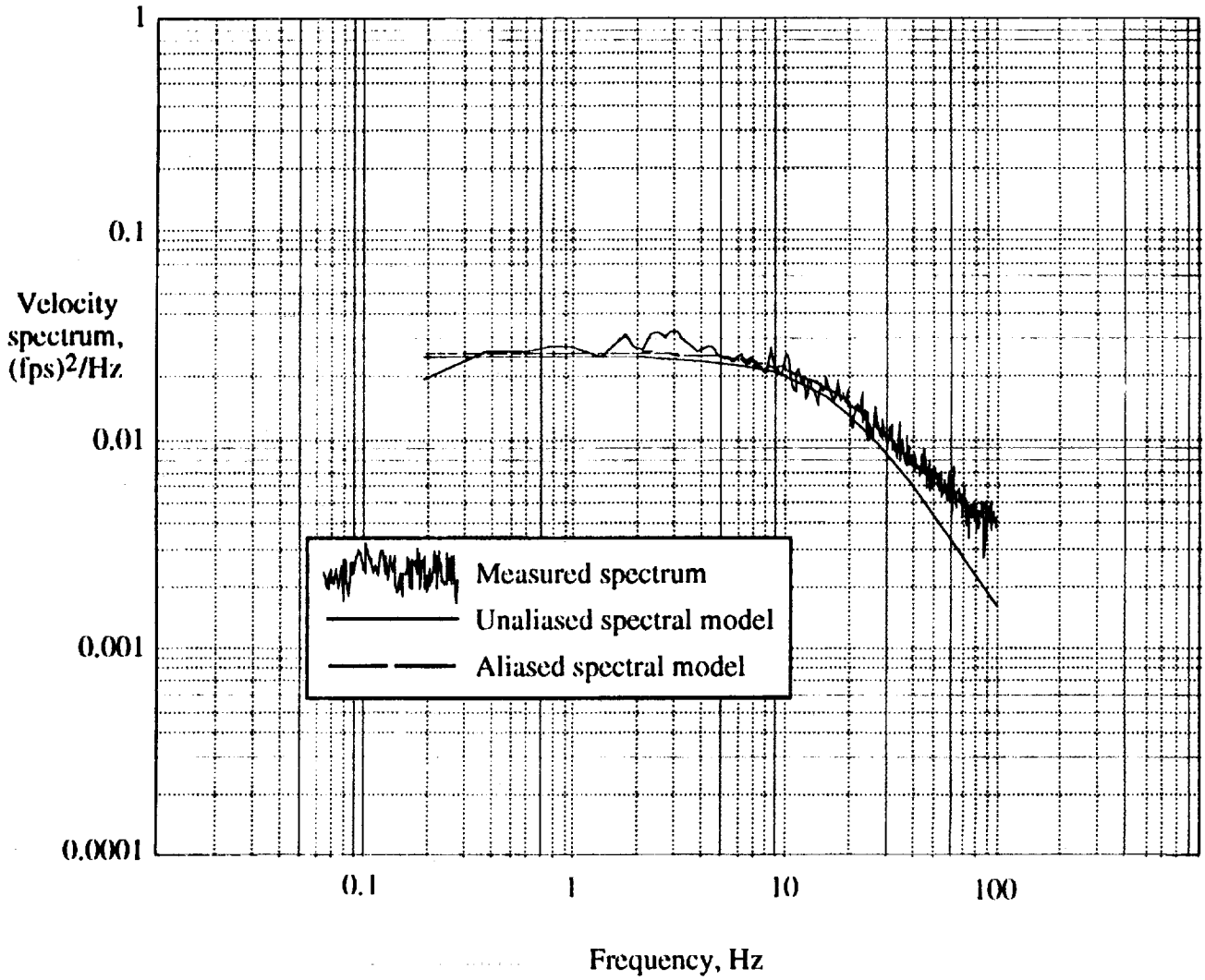

(e) Tunnel velocity 300 fps (tab point 214).

Figure 16. Continued.

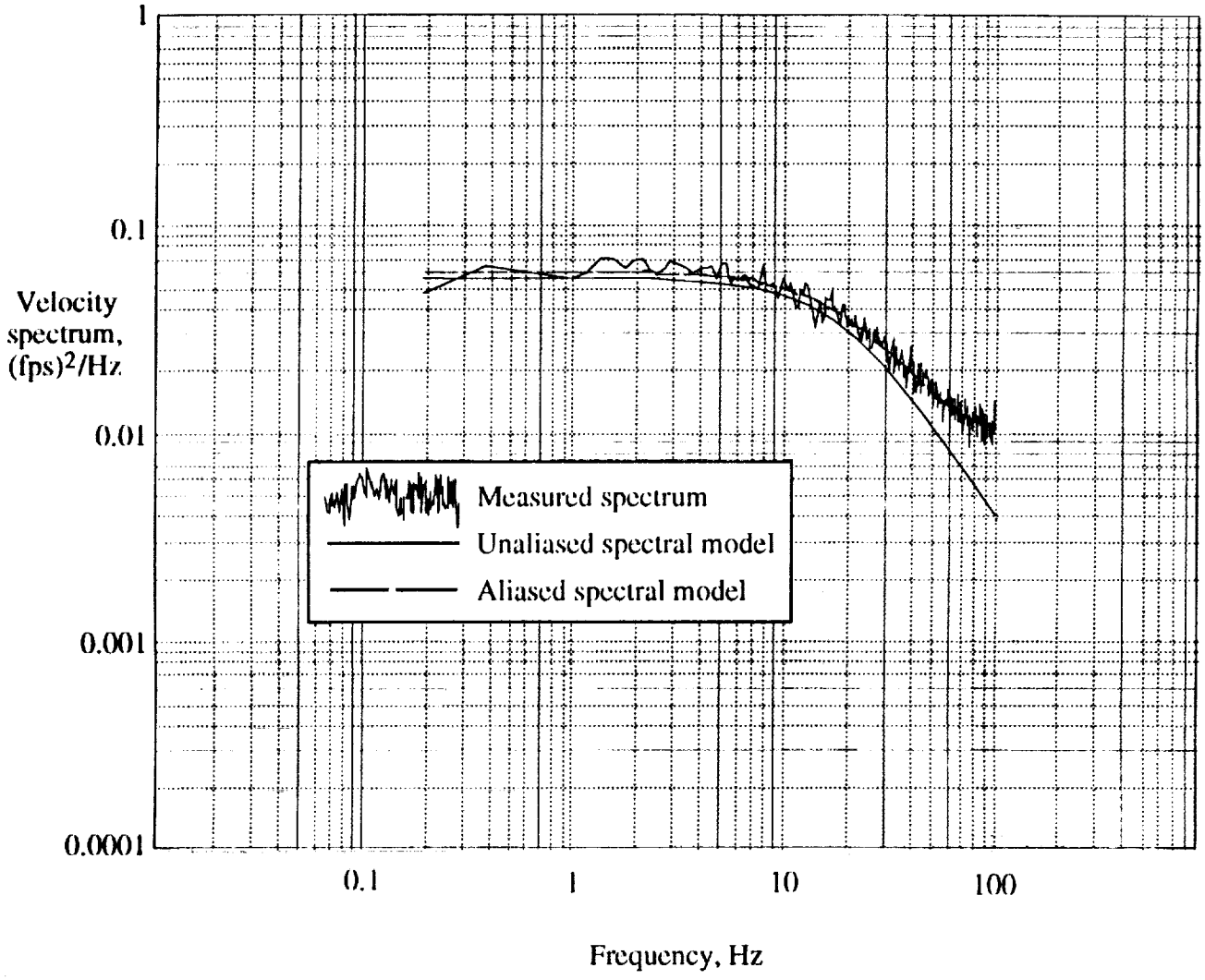

(f) Tunnel velocity 350 fps (tab point 213).

Figure 16. Continued.

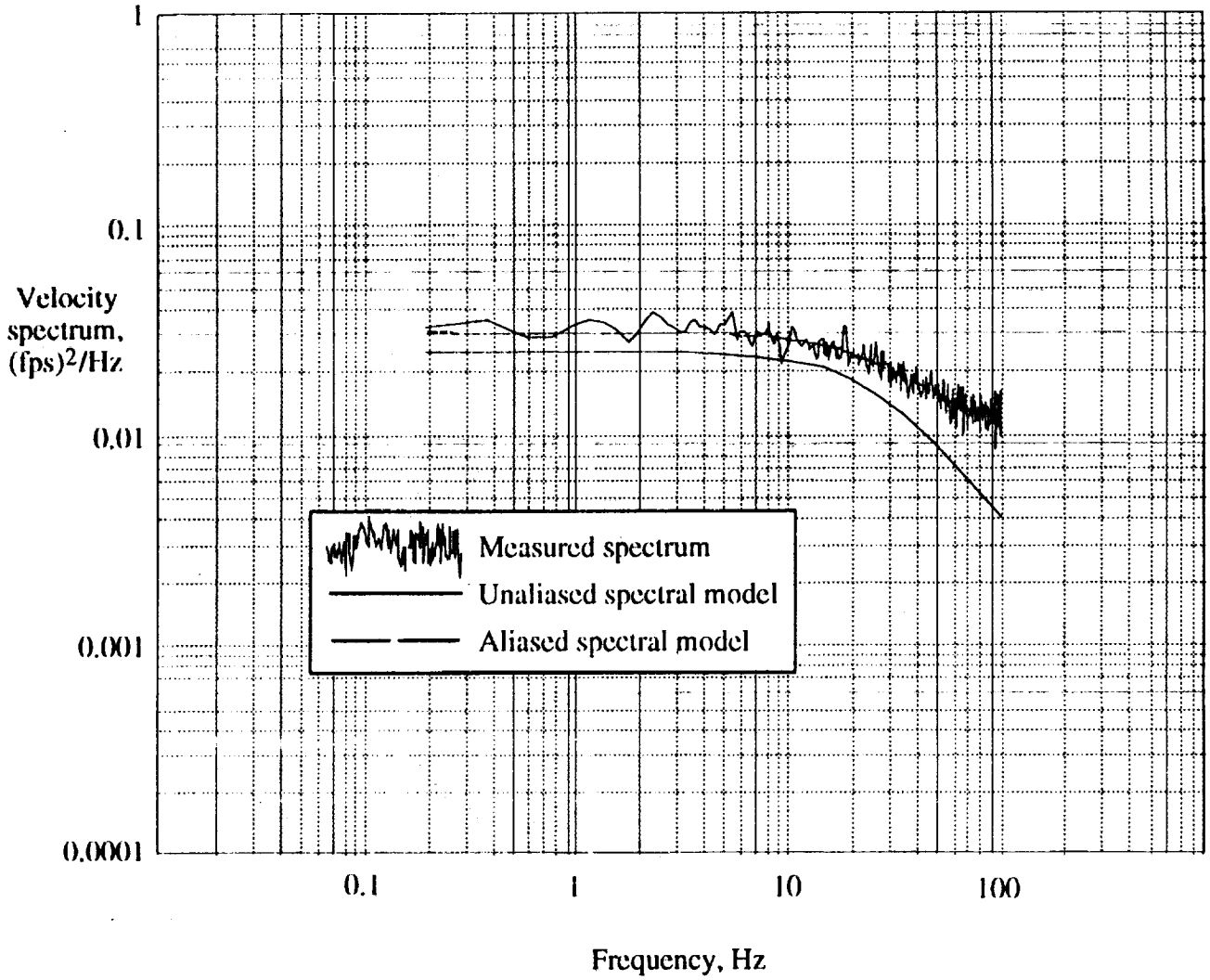

(g) Tunnel velocity 400 fps (tab point 212).

Figure 16. Continued.

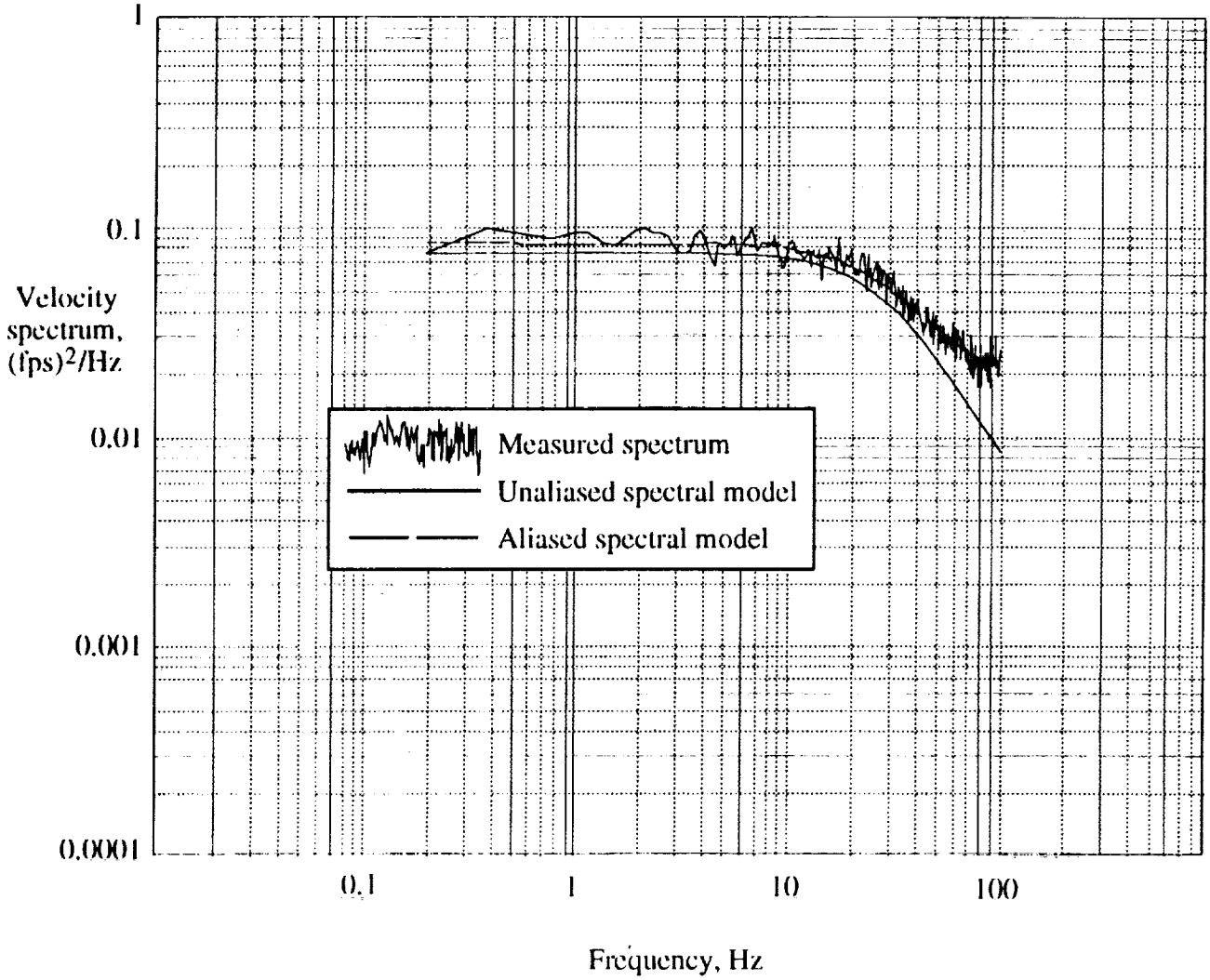

(h) Tunnel velocity 450 fps (tab point 205).

Figure 16. Continued.

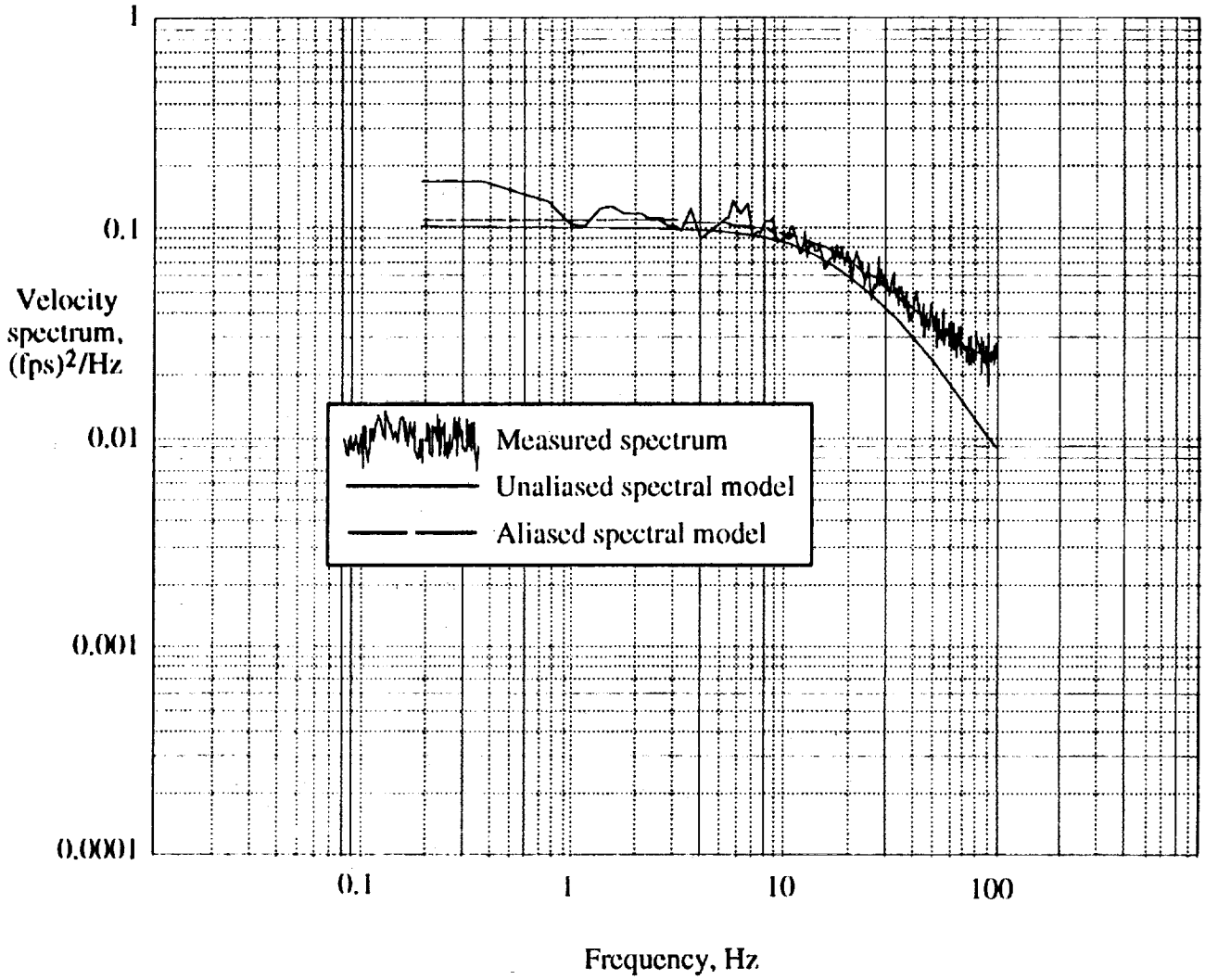

(i) Tunnel velocity 450 fps (tab point 211).

Figure 16. Continued.

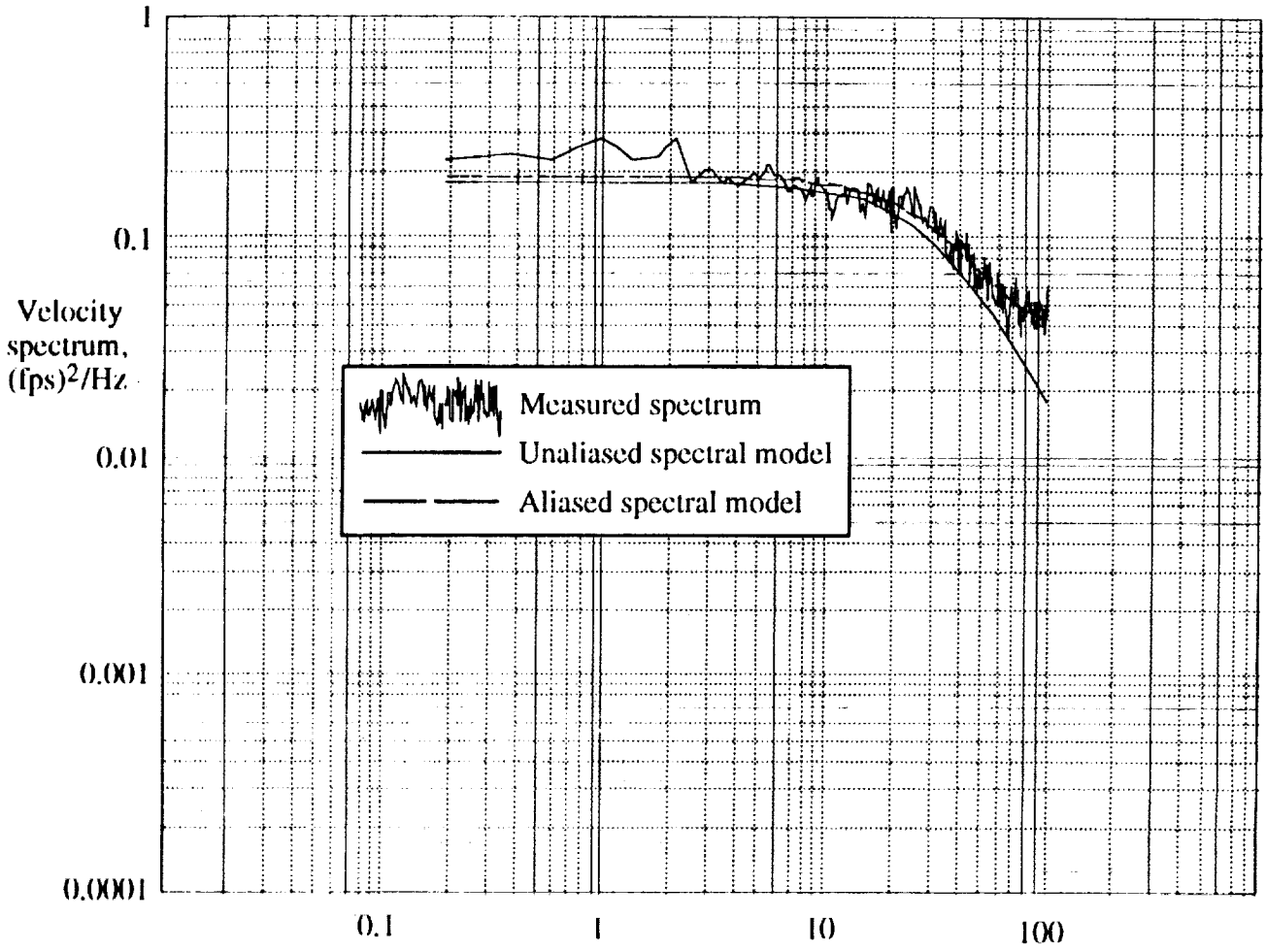

(j) Tunnel velocity 500 fps (tab point 204).

Figure 16. Concluded.

This page left blank intentionally.

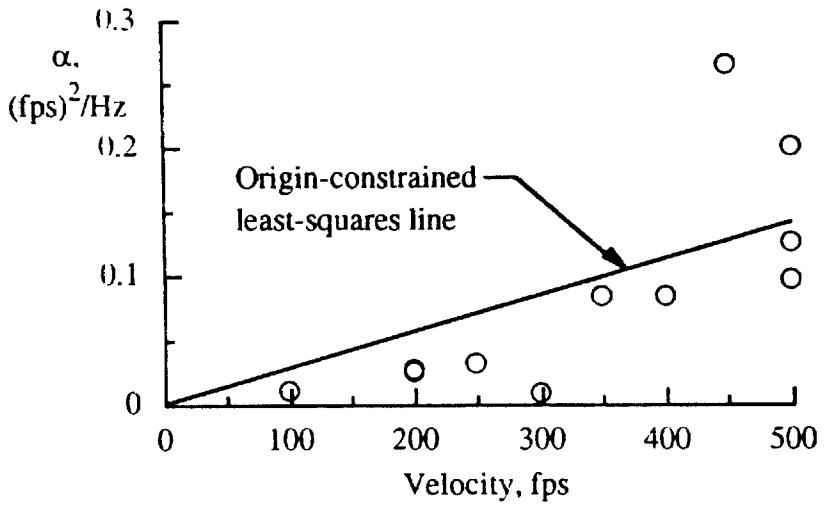

(a) Amplitude, α.

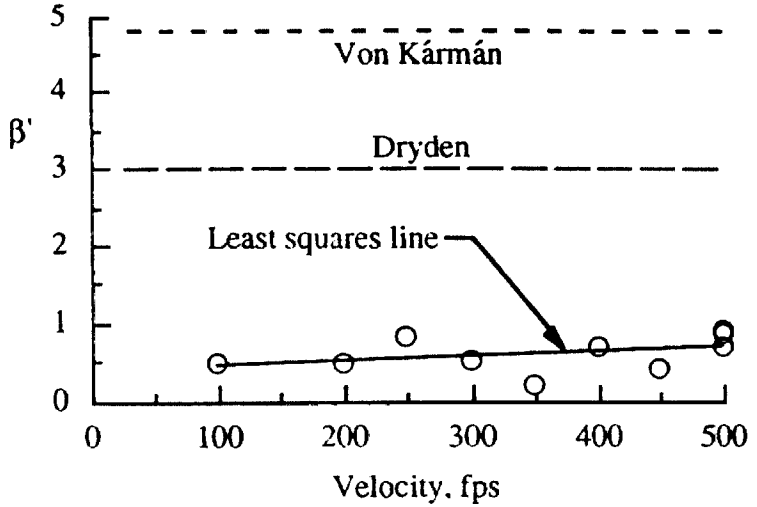

(b) Coefficient, β'.

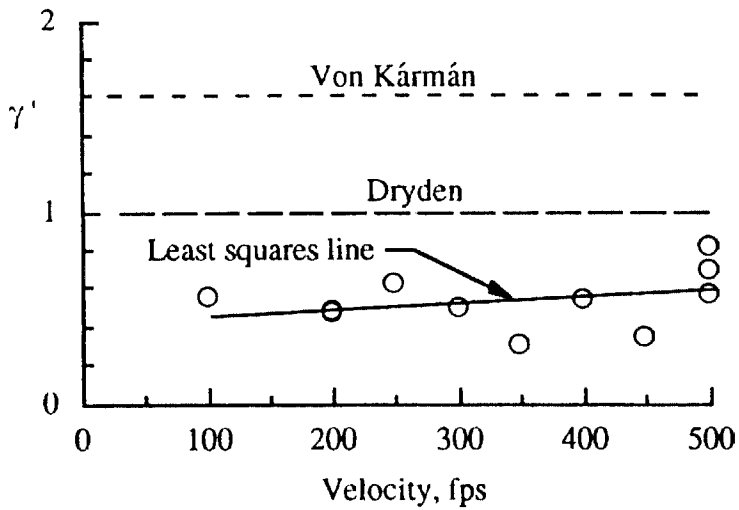

(c) Coefficient, γ'.

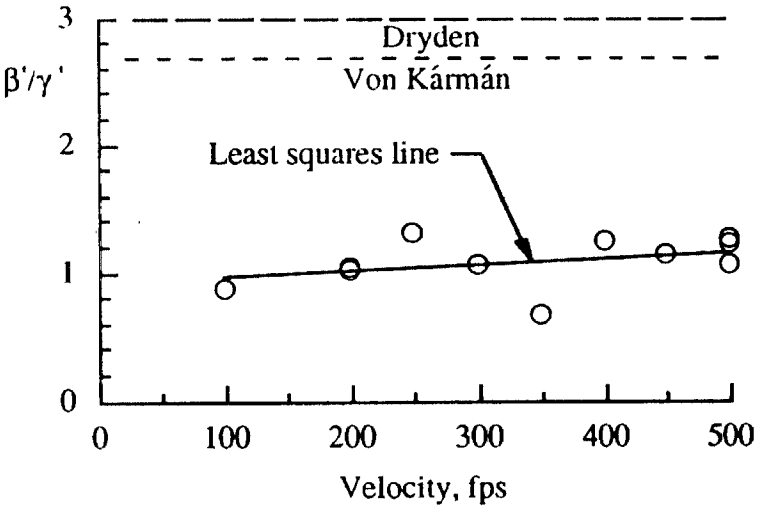

(d) Coefficient ratio, β'/γ'.

Figure 17. Variation of spectral model parameters for the vertical component of tunnel turbulence.

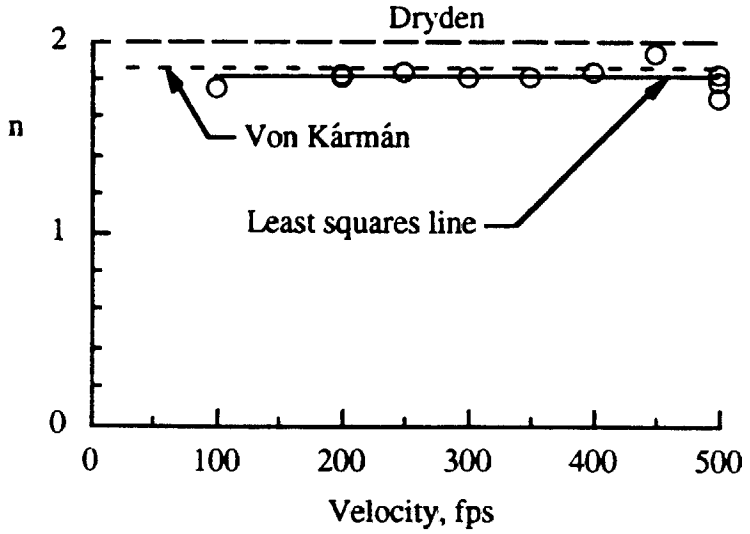

(e) Denominator exponent, n.

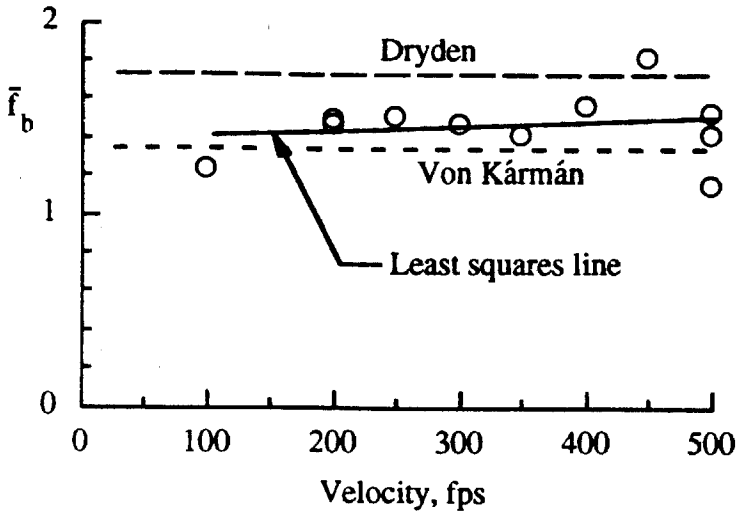

(f) Normalized break frequency, $\bar{f}_b$.

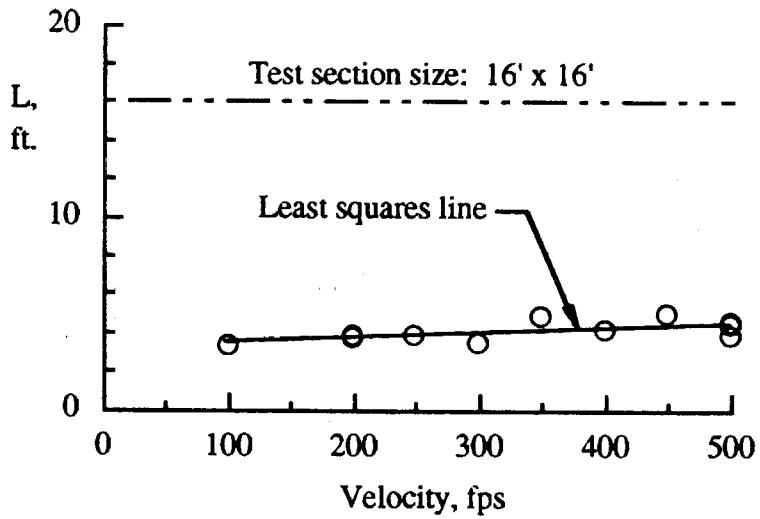

(g) Integral scale length, L.

Figure 17. Concluded.

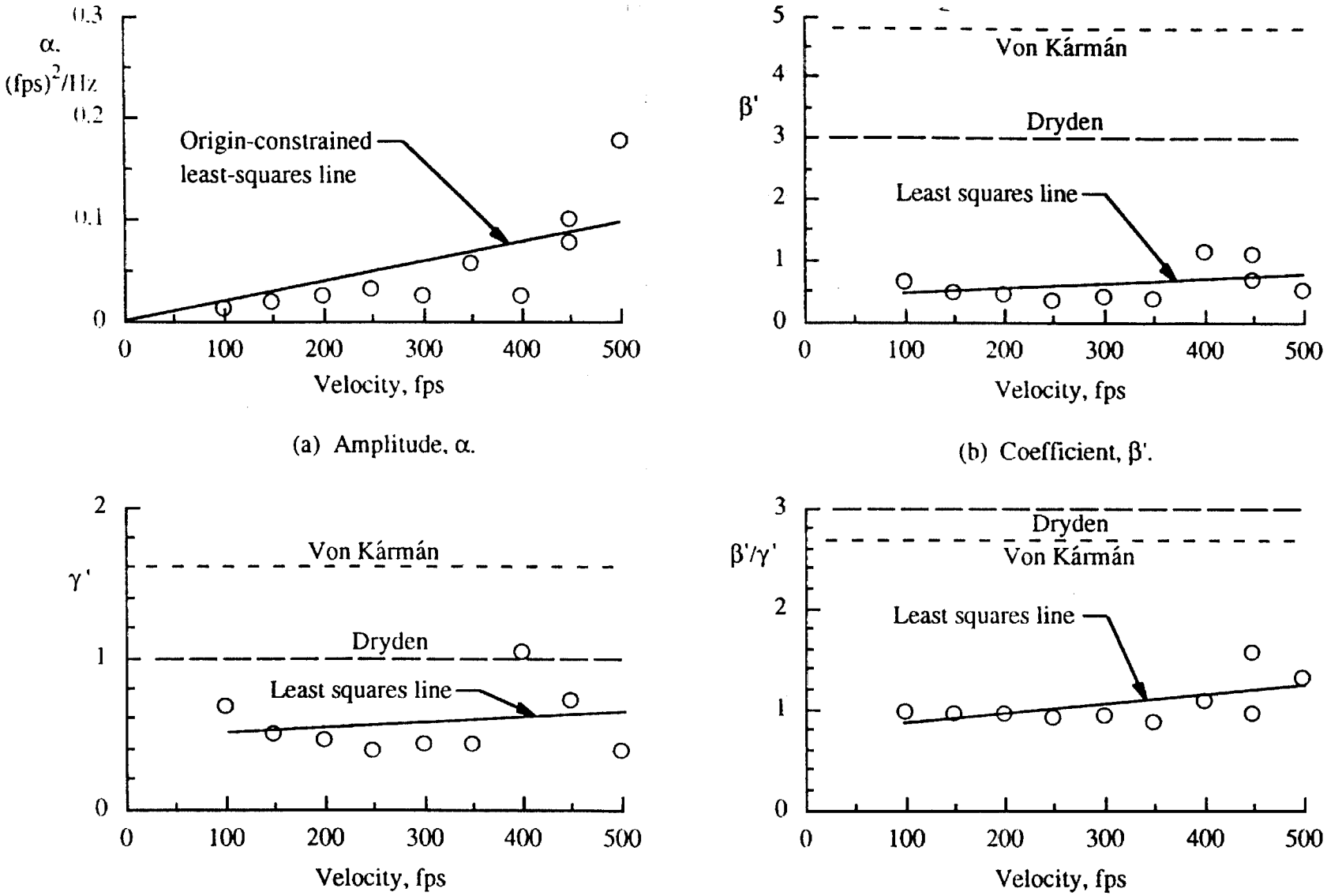

Figure 18. Variation of spectral model parameters for the lateral component of tunnel turbulence.

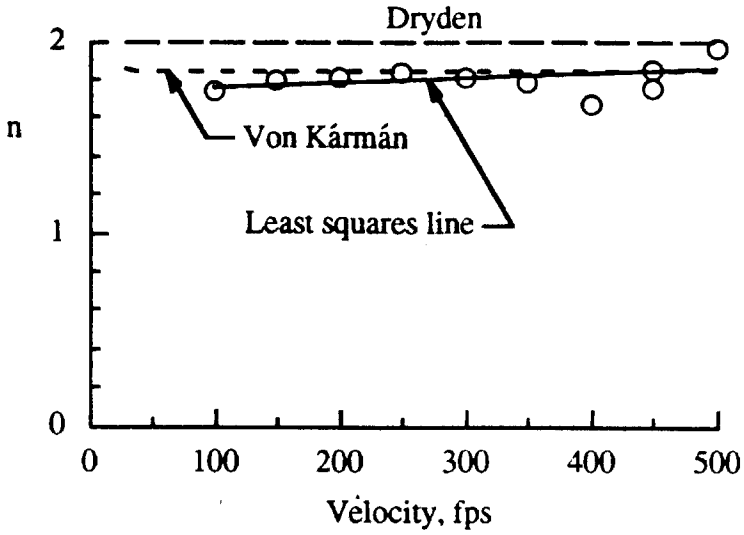

(e) Denominator exponent, n.

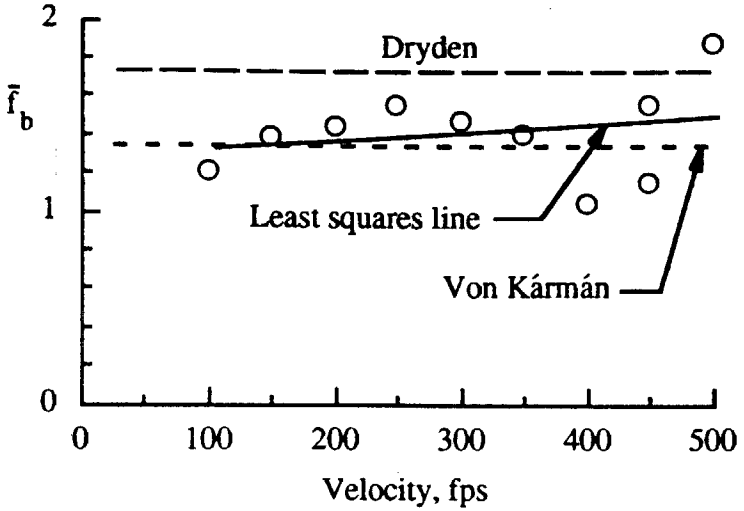

(f) Normalized break frequency, $\bar{f}_b$.

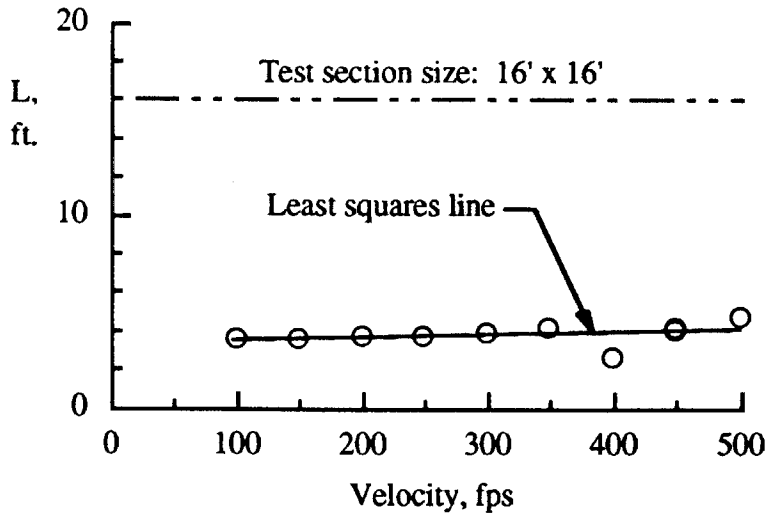

(g) Integral scale length, L.

Figure 18. Concluded.

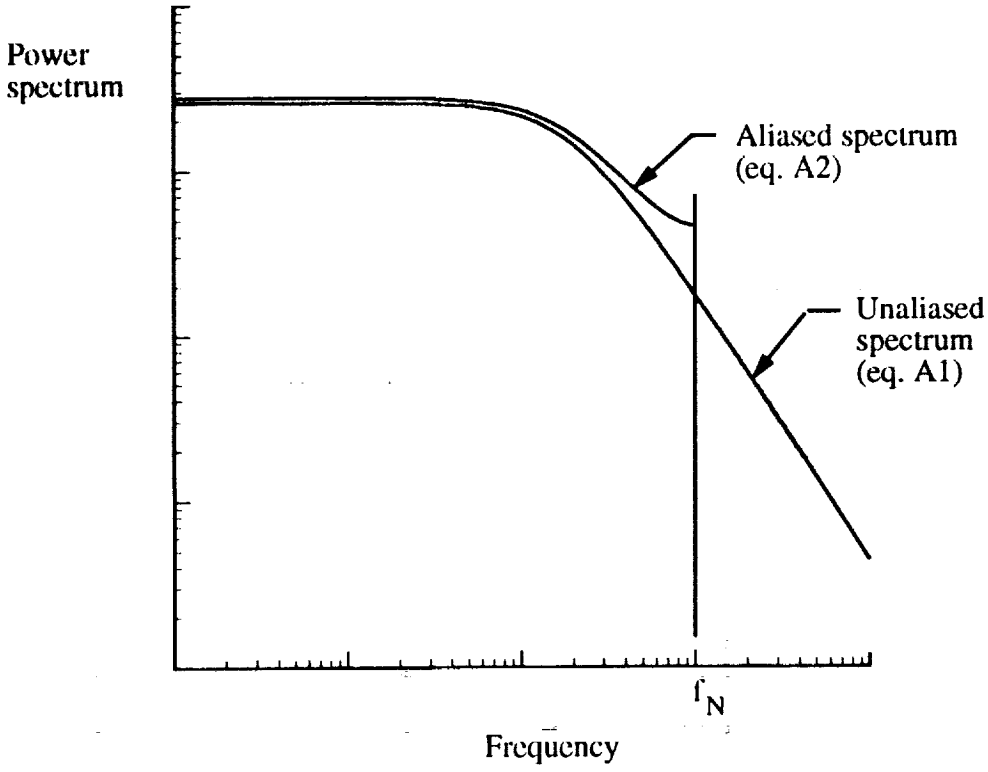

Figure A1. Aliased and unaliased spectral relationships.

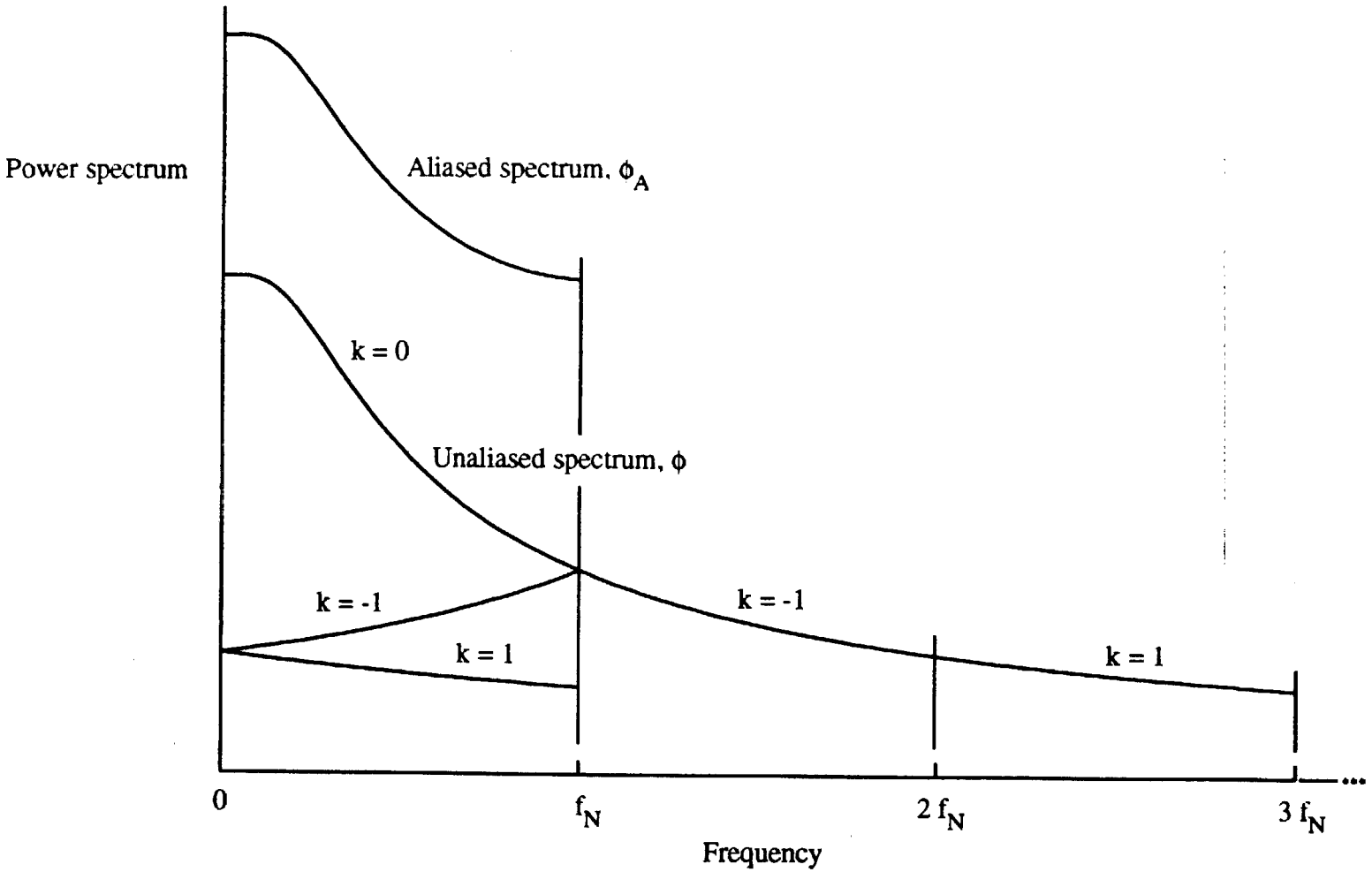

Figure A2. Aliased spectrum composition.

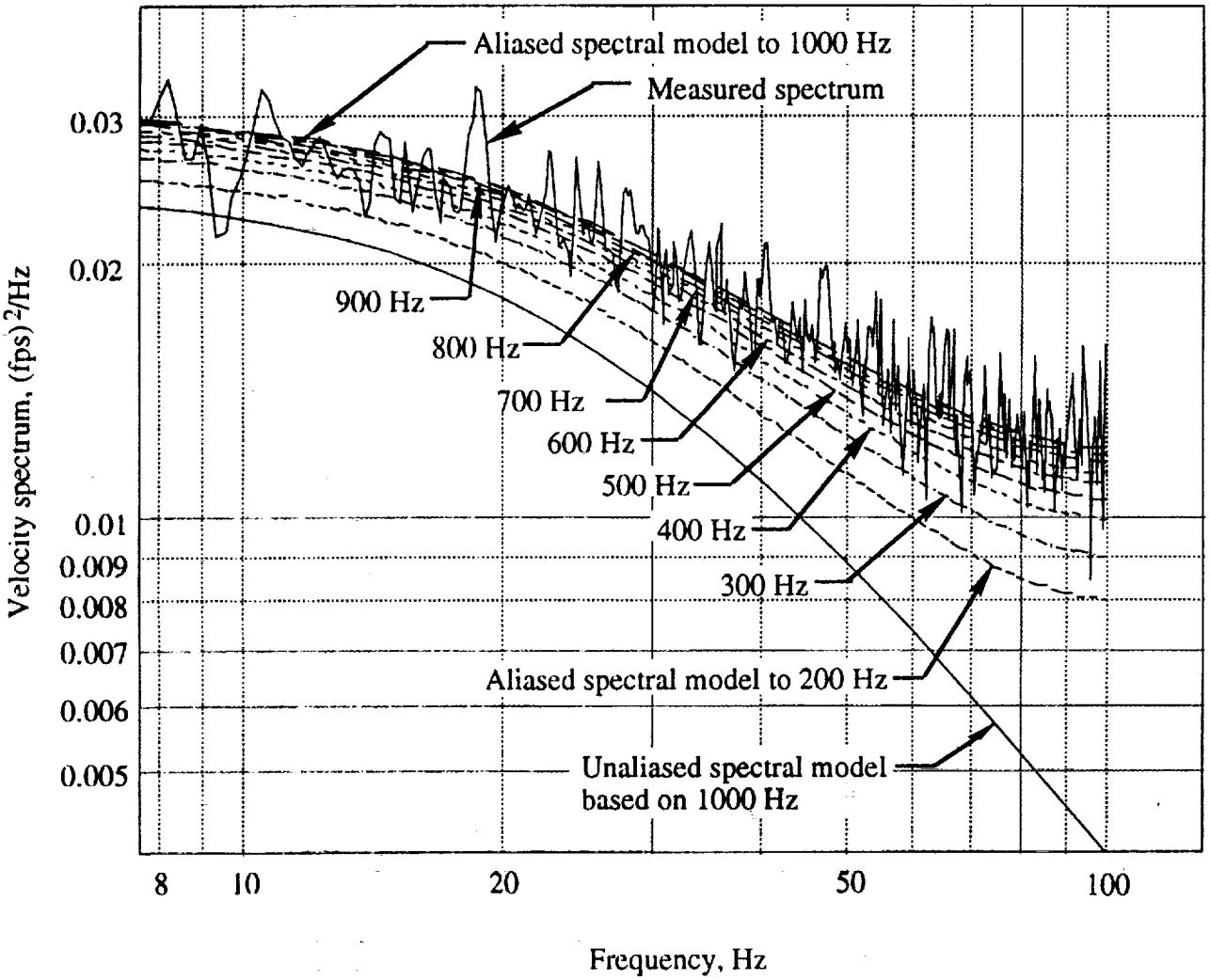

Figure A3. Enlarged high-frequency segment of spectrum.

REPORT DOCUMENTATION PAGE

Form Approved
OMB No 0704-0188

1. AGENCY USE ONLY (Leave blank)	2. REPORT DATE	3. REPORT TYPE AND DATES COVERED
	March 1993	Technical Memorandum

4. TITLE AND SUBTITLE
Characteristics of Vertical and Lateral Tunnel Turbulence Measured in Air in the Langley Transonic Dynamics Tunnel

5. FUNDING NUMBERS
WU 505-63-50-15

6. AUTHOR(S)
Robert K. Sleeper, Donald F. Keller, Boyd Perry III, and Maynard C. Sandford

7. PERFORMING ORGANIZATION NAME(S) AND ADDRESS(ES)
NASA Langley Research Center
Hampton, VA 23681-0001

8. PERFORMING ORGANIZATION REPORT NUMBER

9. SPONSORING / MONITORING AGENCY NAME(S) AND ADDRESS(ES)
National Aeronautics and Space Administration
Washington, DC 20546-0001

10. SPONSORING / MONITORING AGENCY REPORT NUMBER
NASA TM-107734

11. SUPPLEMENTARY NOTES
Similar material to be presented at the Forum on Fluid Measurements and Instrumentation to be held during the ASME 3rd International Symposium on Thermal Anemometry, June 20-24, 1993, in Washington, DC.

12a. DISTRIBUTION / AVAILABILITY STATEMENT
Unclassified - Unlimited

Subject Category 09

12b. DISTRIBUTION CODE

13. ABSTRACT *(Maximum 200 words)*

Preliminary measurements of the vertical and lateral velocity components of tunnel turbulence were obtained in the Langley Transonic Dynamics Tunnel test section using a constant-temperature anemometer equipped with a hot-film X-probe. For these tests air was the test medium. Test conditions included tunnel velocities ranging from 100 to 500 fps at atmospheric pressure. Standard deviations of turbulence velocities were determined and power spectra were computed. Unconstrained optimization was employed to determine parameter values of a general spectral model of a form similar to that used to describe atmospheric turbulence. These parameters, and others (notably break frequency and integral scale length) were determined at each test condition and compared with those of Dryden and Von Kármán atmospheric turbulence spectra. When data were discovered to be aliased, the spectral model was modified to account for and "eliminate" the aliasing.

14. SUBJECT TERMS	15. NUMBER OF PAGES
Wind-tunnel turbulence; Transonic Dynamics Tunnel; turbulence measurements; turbulence spectra; turbulence velocity; vertical and lateral turbulence components; hot-film anemometers	59
	16. PRICE CODE: A04

17. SECURITY CLASSIFICATION OF REPORT	18. SECURITY CLASSIFICATION OF THIS PAGE	19. SECURITY CLASSIFICATION OF ABSTRACT	20. LIMITATION OF ABSTRACT
Unclassified	Unclassified		